

An integrated approach to quantitative modelling in angiogenesis research

Supplementary Material

Anthony J Connor^{*1,7}, Radosław P Nowak^{1,2}, Erica Lorenzon³, Markus Thomas⁴, Frank Herting³, Stefan Hoert³, Tom Quaizer⁵, Eliezer Shochat⁶, Joe Pitt-Francis¹, Jonathan Cooper¹, Philip K Maini⁷, and Helen M Byrne^{1,7}

¹Department of Computer Science, University of Oxford, Oxford, OX1 3QD, UK.

²(Current address) Botnar Research Centre, NIHR Oxford Biomedical Research Unit, Nuffield Department of Orthopaedics, Oxford, OX3 7LD, UK.

³Roche Pharmaceutical Research and Early Development, Oncology DTA, Roche Innovation Center, DE-82377 Penzberg, Germany.

⁴Roche Pharmaceutical Research and Early Development, Discovery Ophthalmology, Roche Innovation Center, 4070 Basel, Switzerland.

⁵Roche Pharmaceutical Research and Early Development, pRED Informatics, Roche Innovation Center, DE-82377 Penzberg, Germany.

⁶Roche Pharmaceutical Research and Early Development, Roche Innovation Center, 4070 Basel, Switzerland.

⁷Wolfson Centre for Mathematical Biology, Mathematical Institute, University of Oxford, Oxford, OX2 6GG, UK.

Contents

1	Semi-automated vessel segmentation in cornea micropocket images	2
2	Mathematical model of corneal angiogenesis	5
3	Parameter value estimation	14
4	Mathematical model implementation	21
5	Parameter sensitivity analysis	21
6	Numerical convergence	23

* Author for correspondence: anthony.connor@keble.ox.ac.uk.

1 Semi-automated vessel segmentation in cornea micropocket images

In our study we analysed images from 9 experiments in which pellets containing 300 ng of VEGF-A₁₆₅ were implanted into the corneas of mice, and 10 experiments in which 15 ng of bFGF was used. The process of vascular network extraction is subdivided into a series of semi-automated procedures which we partition into pre-processing, enhancement, post-processing and segmentation steps, and describe below (see also Figure S1). For simplicity, throughout our analysis we neglect the effect of the curvature of the eye.

i) **Pre-processing**

To obtain a scale for the images we assume that each mouse has a spherical eye of radius 1.53 mm, as suggested by Rogers *et al.* [S1] and confirmed by measurements made at Hoffmann-La Roche, Penzberg. We fit a circle to a selection of ten points placed manually around the circumference of the exposed portion of the eye in each image and measure the circumference of that circle in terms of pixels. This allows us to estimate the scale (number of pixels per mm) for each image.

The image is manually cropped to a rectangular region which identifies the central portion of the cornea. In this region the vasculature is most in focus and therefore most amenable to segmentation. The cropped image is then rotated (usually by a few degrees) in order to align the limbal vessel(s) with the horizontal axis of the image. At this point the closest distance between the pellet and the limbal vessels is measured. In this way, we obtain an estimate for the distance that the pellet is placed away from the limbal vessels.

ii) **Enhancement**

The vasculature in each image is enhanced using an adaptation of the Gaussian matched filter approach first introduced by Chaudhuri *et al.* [S2]. The matched filter approach to vessel enhancement is a template-matching algorithm, the success of which relies on the assumption that vessels have a predictable intensity profile. An acceptable assumption is that the cross-sectional intensity profile of a vessel is approximately Gaussian. We confirmed this for our set of cornea images. The filters are extended to two dimensions by assuming that vessels usually have small curvatures and thus can be approximated by small piecewise linear segments. Thus, each matched filter kernel may be expressed as

$$k(x, y) = -\exp\left(-\frac{x^2}{2\sigma^2}\right) \quad \forall \quad |y| \leq \frac{L}{2}, \quad (\text{S1})$$

where L is the length over which the vessel is assumed to have a fixed orientation. Since vessels may appear in any orientation, the filter is rotated through all possible angles ($0 \leq \theta \leq \pi$) to produce a bank of filters, k_i , of fixed size.

To limit the size of the matched filters, the Gaussian curves are truncated at $\pm T$ pixels. Furthermore, the kernel is modified by subtracting the mean value of $k(x, y)$ so that when the kernel is applied to a pixel belonging to a background of constant intensity, with zero mean

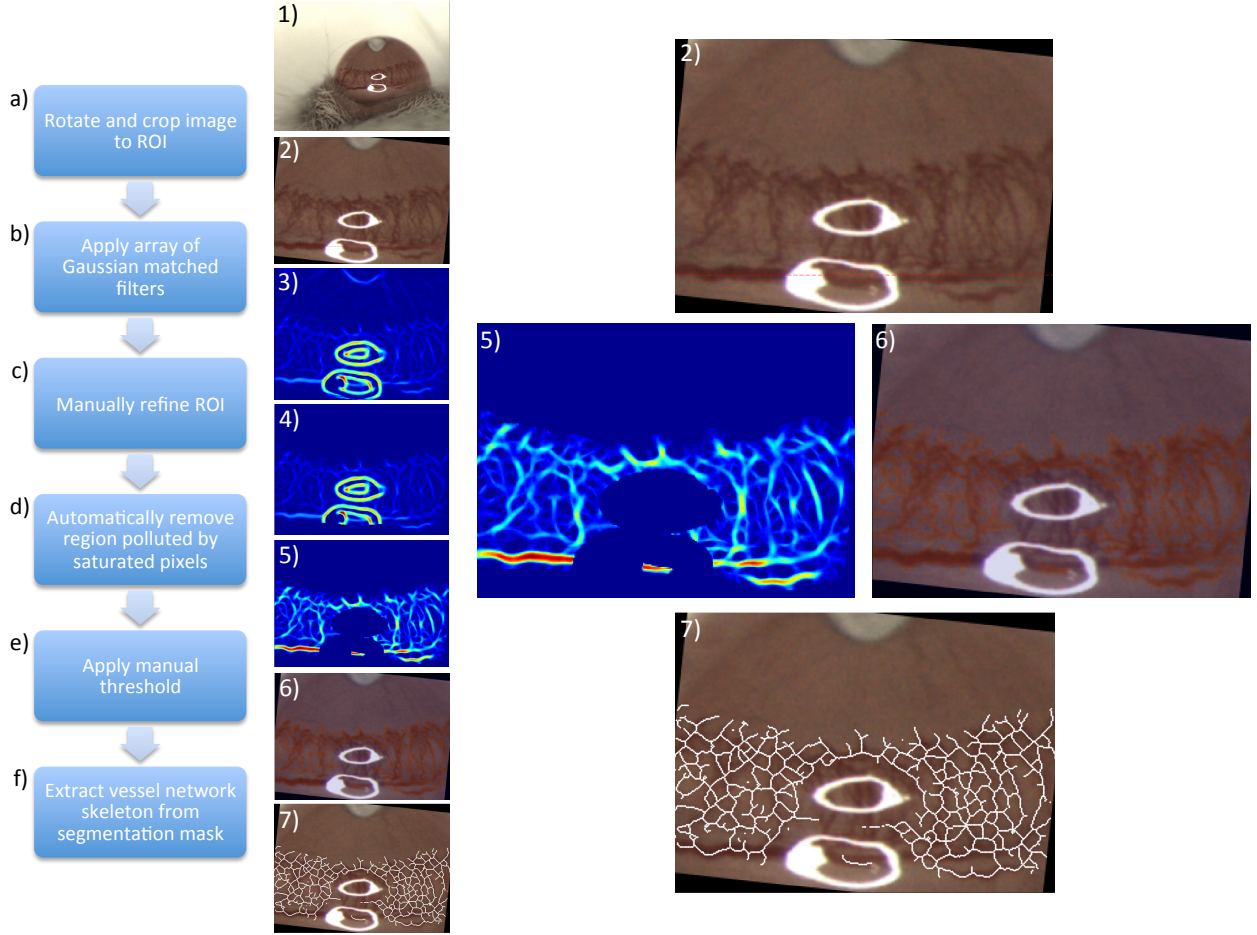


Figure S1: Work flow for vessel extraction from cornea micropocket assay images. See main text for details.

additive noise, the response will be zero. Thus, we have

$$k'_i(x, y) = k_i(x, y) - \frac{1}{a} \sum_{x, y} k_i(x, y), \quad (\text{S2})$$

where a is the number of elements in the discrete implementation of the filter.

The vessel enhancement algorithm proceeds by convolving each matched filter kernel, k_i , with the image to produce an array of matched filter responses, M_i . The final matched filter response, M , is obtained by retaining the maximal matched filter response over all orientations for each pixel, i.e. $M(x, y) = \max_i M_i(x, y)$.

We extend the matched filter approach presented above, considering an extended bank of Gaussian matched filters of varying σ . By including filters of smaller width we increase the matched filter response to smaller vessels and thus increase the likelihood that these vessels will be identified in a subsequent segmentation step.

To parameterise our matched filter method we largely follow Al-Rawi *et al.* [S3], who performed a search of the parameter space (σ, L, T) in an attempt to optimise the Gaussian matched filter method for retinal images. L is fixed at 11 pixels and σ is varied between 0.5

and 2 in steps of 0.1. As σ is varied, T is also varied, such that $T = 4\lceil\sigma\rceil$, consistent with [S3]. The angular resolution of the bank of filters is fixed at 15° .

iii) **Post-processing**

We refine our region of interest (ROI) to the area in which the vascular growth is localised by drawing around it manually. This eliminates the potential for spurious signals to appear in the matched filter response due to background noise in the region between the neovasculature and the pellet. We also eliminate saturated regions from each image by thresholding a Hue-Saturation-Value (HSV) representation of the image according to each pixel's associated V-value.

After refining the ROI, the pixel values in the enhanced image are renormalised such that pixels which are most likely to correspond to a vessel are given a value of 255 and pixels which are least likely to correspond to a vessel are given a value of zero. Figure S1 (image 5) shows an example of a finalised enhanced image resulting from this process.

iv) **Segmentation**

To segment the vasculature from the background image we apply a threshold to the enhanced image. An automated thresholding procedure, known as local entropy thresholding, provides an initial segmentation of the vascular network [S4]¹. The initial threshold level is tuned by eye in order to improve the accuracy of the network segmentation, where possible. An example final binary segmentation of the vasculature from an image is shown in Figure S1 (image 6).

After thresholding, we apply a thinning procedure, via MATLAB's *bwmorph* function, to reveal the back-bone, or skeleton, of the vascular network. This skeleton provides an approximate but reasonably comprehensive indication of the locations of the centre-lines of the vessels in our images. An example vessel network skeleton is illustrated in Figure S1 (image 7).

In the model developed in this paper the vascular density is averaged in the plane perpendicular to the direction in which the vascular front is moving on average (from the limbus to the pellet). Thus, to compare model simulations with the experimental data, we perform a similar averaging here; using our skeletonised networks, we count the number of identified vessels along each plane perpendicular to the direction in which vascular growth occurs on average, i.e. we count vessels along the x-direction in our images (see Figure 2e in the main manuscript). We use these vessel counts to estimate the average vascular density, measured in metres of vessel per metre cubed, at all locations between the pellet and limbus. In our calculation of vascular density, we assume that the corneal stroma has a thickness of approximately $100\mu\text{m}$ as suggested in [S5, S6]. These data are used to produce a plot, or a vascular density profile, which describes how the vascular density varies on average across each cornea image, moving from the limbal vessels towards the pellet. This process is fully automated.

For each set of experiments the vascular density profiles were concatenated and averaged so that we might evaluate the average neovascular response of the corneal vasculature to each angiogenic factor at their respective doses. The resulting averaged spatially-resolved and dynamic data are used

¹We use an implementation for the local entropy thresholding algorithm as provided by Chanwimaluang and Fan at <http://www.vcipl.okstate.edu/localentropy.htm>. Our Gaussian matched filter implementation has also been adapted from that of Chanwimaluang and Fan, hosted at the same address.

to parameterise our model and compare the angiogenic responses elicited by VEGF-A₁₆₅ and bFGF pellets.

MATLAB scripts are available which allow for efficient reproduction of the image processing results, presented in the main manuscript. These scripts may be found at [S7] with accompanying experimental images at [S8].

2 Mathematical model of corneal angiogenesis

An overview of our mathematical model was presented in the main manuscript. In this section we elaborate upon the equations underlying our mathematical model. We consider dependent variables which represent averages in the plane perpendicular to the average direction of sprout tip motion, thus restricting attention to one spatial dimension. The independent variables in our model are time, t , and space, x , where the x -axis lies parallel to the average direction of tip cell motion, with limbus located at $x = 0$ and the pellet at $x = L$. We develop equations for the average density of sprout tips, $n(x, t)$, the average length density of immature vessels, $\rho(x, t)$, the average length density of mature vessels, $m(x, t)$, the average concentration of VEGF-A₁₆₅, $v(x, t)$, and the average concentration of bFGF, $f(x, t)$. We also model the mean concentration of VEGF-A₁₆₅ and bFGF in the pellets, denoted $[V_T](t)$ and $[F_T](t)$, respectively. See Table S1 for a summary of the dependent variables. We begin by developing equations in which explicit crosstalk between VEGF-A₁₆₅ and bFGF is not taken into account. We then adapt those equations to account for crosstalk between the two factors.

2.1 Mature vessel density equation, $m(x, t)$

Vessel maturation and dematuration are complex processes involving many chemical species and multiple cell types. Such details have been incorporated into recent models by Zheng *et al.* [S9]. However, we take a simplified approach to modelling vessel maturity which is appropriate for the coarse-grained data which our experimental images provide. We assume VEGF-A₁₆₅ binding to ECs induces vessel dematuration at a rate proportional to the fraction of bound VEGFR-2 receptors, further assuming Michaelis-Menten reaction kinetics. Similarly, bFGF binding to FGFR-1 induces vessel dematuration. Meanwhile, since maturation is expected to take place on a longer time scale than dematuration, and little maturation is expected to take place in bFGF and VEGF-A₁₆₅ experiments [S10], to simplify our model we neglect vessel maturation. Based on evidence presented in [S11], mature vessels are viewed as immobile and stable, and only dematuration is assumed to contribute to their evolution. Combining these assumptions, the equation governing the mature vessel density, m , is given by:

$$\frac{\partial m}{\partial t} = - \underbrace{\left(\frac{\lambda_1^v v}{v + v_{\frac{1}{2}}} + \frac{\lambda_1^f f}{f + f_{\frac{1}{2}}} \right)}_{\text{dematuration}} m \quad (\text{S3})$$

λ_1^v and λ_1^f are the maximal rates of vessel dematuration due to VEGF-A₁₆₅ and bFGF, respectively. $v_{\frac{1}{2}}$ is the concentration of VEGF-A₁₆₅ at which half of the VEGFR-2 receptors are bound, and $f_{\frac{1}{2}}$ is the concentration of bFGF at which half of the FGFR-1 receptors are bound.

Variable	Description	Units
n	Number of sprout tips per unit volume, averaged in the plane perpendicular to direction of tip migration.	tips m^{-3}
ρ	Length of immature vessels per unit volume, averaged in the plane perpendicular to direction of tip migration.	m of vessel m^{-3}
m	Length of mature vessels per unit volume, averaged in the plane perpendicular to direction of tip migration.	m of vessel m^{-3}
v	Mean molar concentration of VEGF-A ₁₆₅ across cross-sectional area of cornea.	M
f	Mean molar concentration of bFGF across cross-sectional area of cornea.	M
$[V_T]$	Mean concentration of VEGF-A ₁₆₅ inside pellet.	M
$[F_T]$	Mean concentration of bFGF inside pellet.	M

Table S1: Table of dependent variables.

2.2 Sprout tip density equation, $n(x, t)$

Both VEGF-A₁₆₅ and bFGF binding in immature vessels stimulates the production of sprout tips. The rate at which new tips form from existing immature vessels in response to VEGF-A₁₆₅ is assumed proportional to the local fraction of bound VEGFR-2. Similarly, the rate at which new tips form in response to bFGF is proportional to the local fraction of bound FGFR-1. Following [S12, S13], sprout tips move via chemotaxis (in response to gradients in both VEGF-A₁₆₅ and bFGF) and also undergo random motion. Tips are annihilated when they anastomose with vessels or other tips. Additionally, tips die in low concentrations of VEGF-A₁₆₅ and bFGF. In summary, the governing equation for tip density, $n(x, t)$, is given by:

$$\begin{aligned}
\frac{\partial n}{\partial t} = & \frac{\partial}{\partial x} \left(\underbrace{\mu \frac{\partial n}{\partial x}}_{\text{random motion}} - \underbrace{\chi_f n \frac{\partial f}{\partial x} - \chi_v n \frac{\partial v}{\partial x}}_{\text{chemotaxis}} \right) + \underbrace{\alpha_0^v \left(\frac{v}{v + v_{\frac{1}{2}}} \right) \rho + \alpha_0^f \left(\frac{f}{f + f_{\frac{1}{2}}} \right) \rho}_{\text{sprouting from vessels}} \\
& - \underbrace{\beta_1 (\rho + m) n}_{\text{tip-to-vessel anastomosis}} - \underbrace{2 \beta_2 n^2}_{\text{tip-to-tip anastomosis}} - \underbrace{\gamma n \left(\frac{v_{\frac{1}{2}}}{v + v_{\frac{1}{2}}} \right) \left(\frac{f_{\frac{1}{2}}^f}{f + f_{\frac{1}{2}}^f} \right)}_{\text{death}}, \tag{S4}
\end{aligned}$$

where μ , χ_f and χ_v are the random motility and chemotactic coefficients, respectively. α_0^v and α_0^f are the maximal rates of VEGF-A₁₆₅- and bFGF-induced production of tips per length of immature vessel, respectively. β_1 is the rate of tip-to-vessel anastomosis per unit vessel length density per unit tip density per unit volume, β_2 is the rate of tip-to-tip anastomosis per unit tip density squared per unit volume and γ is the maximal rate of EC death in low VEGF-A₁₆₅ and bFGF conditions. All parameters are assumed non-negative and constant.

2.3 Immature vessel density equation, $\rho(x, t)$

We again follow [S12, S13], wherein the production of immature vessels is modelled using the snail-trail approach. As mentioned in the main manuscript and Section 2.2, above, we assume that the ECs associated with immature vessels rely on angiogenic factors for survival. Therefore, in the absence of VEGF-A₁₆₅ and bFGF, immature vessels regress. By contrast, mature vessels do not rely on external sources of angiogenic factors for their viability and, as a result, do not undergo regression when VEGF-A₁₆₅ and/or bFGF is withdrawn [S14]. In summary, the immature vessel

length density, $\rho(x, t)$, obeys the following PDE:

$$\begin{aligned} \frac{\partial \rho}{\partial t} = & \underbrace{\kappa \left[\mu \frac{\partial n}{\partial x} - \chi_f n \frac{\partial f}{\partial x} - \chi_v n \frac{\partial v}{\partial x} \right]}_{\text{snail-trail}} - \underbrace{\gamma \rho \left(\frac{v_{\frac{1}{2}}}{v + v_{\frac{1}{2}}} \right) \left(\frac{f_{\frac{1}{2}}^f}{f + f_{\frac{1}{2}}^f} \right)}_{\text{regression}} \\ & + \underbrace{\left(\frac{\lambda_1^v v}{v + v_{\frac{1}{2}}} + \frac{\lambda_1^f f}{f + f_{\frac{1}{2}}^f} \right) m}_{\text{dematuration}}, \end{aligned} \quad (\text{S5})$$

where we have also included terms for vessel dematuration to ensure appropriate conservation of the total vessel length density in our equations. The constant κ quantifies the length of vessel left behind as a sprout tip migrates towards the pellet. Setting $\kappa > 1$ allows us to account for some production of vessel length in the plane perpendicular to the x -axis.

2.4 VEGF-A₁₆₅ concentration equation, $v(x, t)$

The VEGF-A₁₆₅ distribution in our system is assumed to depend upon diffusion, natural decay, uptake by ECs and drainage through the vasculature. Combining these assumptions, we propose the following equation for the evolution of the VEGF-A₁₆₅ distribution in our model domain:

$$\frac{\partial v}{\partial t} = \underbrace{D_v \frac{\partial^2 v}{\partial x^2}}_{\text{diffusion}} - \underbrace{\lambda_v v}_{\text{natural decay}} - \underbrace{2 \pi \bar{R} P_v (\rho + m) v}_{\text{drainage through vessels}} - \underbrace{K_{EC}^v (\rho + m) \left(\frac{v}{v + v_{\frac{1}{2}}} \right)}_{\text{uptake via endothelial cells}}. \quad (\text{S6})$$

In (S6), D_v is the assumed constant diffusion coefficient for VEGF-A₁₆₅ in the corneal stroma and λ_v is the rate constant for natural decay. For simplicity, we assume that the permeability of vessels to VEGF-A₁₆₅, P_v , is constant and all vessels have the same radius, \bar{R} . Additionally, we assume that the maximal rate at which ECs in vessels uptake VEGF-A₁₆₅ is K_{EC}^v .

The third term in (S6) represents the rate of loss of VEGF-A₁₆₅ per unit volume due to the outward flux of VEGF-A₁₆₅ through vessel walls. We approximate vessels as cylinders and therefore assume that the surface area for VEGF-A₁₆₅ exchange per unit volume is given by $2 \pi \bar{R} (\rho + m)$. The flux of VEGF-A₁₆₅ crossing a vessel wall, measured in moles per unit time per unit area of vessel wall, is assumed proportional to the difference in molar concentration of VEGF-A₁₆₅ on either side of the wall. We also assume that the concentration of VEGF-A₁₆₅ inside a vessel is negligible. The uptake of VEGF-A₁₆₅ by ECs is described by the fourth term on the RHS of (S6), where we have neglected the contribution of tip cells to the uptake of VEGF-A₁₆₅. While VEGF-A₁₆₅ binds to a number of receptors on the surface of cells, for simplicity we account only for VEGF-A₁₆₅ binding to VEGFR-2 molecules. The absence of a source term on the RHS of (S6) reflects our assumption that VEGF-A₁₆₅ is only released into the cornea from the pellet. Thus, the influx of VEGF-A₁₆₅ into the cornea is incorporated via a boundary condition at $x = L$, which we discuss below.

2.5 bFGF concentration equation, $f(x, t)$

We model the bFGF distribution in a similar way to the VEGF-A₁₆₅ distribution. Similar to VEGF-A₁₆₅, bFGF binds to a number of receptors on the surface of cells and to various elements of the corneal stroma. However, for simplicity we incorporate only bFGF/FGFR-1 binding in our model since bFGF regulates EC behaviour principally by binding to FGFR-1 receptors. We also account for diffusion, natural decay and drainage through the vasculature. Thus, we model the evolution of bFGF concentration in our model using the equation:

$$\frac{\partial f(x, t)}{\partial t} = \underbrace{D_f \frac{\partial^2 f}{\partial x^2}}_{\text{diffusion}} - \underbrace{\lambda_f f}_{\text{natural decay}} - \underbrace{2 \pi \bar{R} P_f (\rho + m) f}_{\text{drainage into vascular system}} - \underbrace{K_{EC}^f (\rho + m) \left(\frac{f}{f + f_{\frac{1}{2}}^f} \right)}_{\text{uptake via FGFR-1}}. \quad (\text{S7})$$

Here, $f_{\frac{1}{2}}^f$ is as defined above and K_{EC}^f represents the maximal rate of reduction in bFGF concentration due to cellular uptake via FGFR-1. Other parameters in (S7) parallel those defined for VEGF-A₁₆₅ transport in (S6).

2.6 VEGF-A₁₆₅/bFGF crosstalk

bFGF is thought to induce angiogenesis upstream of VEGF-A, and partly via the VEGF-A/VEGFR-2 pathway [S15]. More specifically, exposure to bFGF upregulates the expression of VEGFR-2 [S16] and stimulates ECs to produce VEGF-A [S17]. In our model we incorporate these mechanisms of crosstalk.

Since we do not model VEGFR-2 density explicitly, increases in VEGFR-2 density are reflected in the transient modulation of a number of parameter values. We assume that exposure to bFGF leads to increased uptake of VEGF-A₁₆₅ by ECs, increased VEGF-A₁₆₅-induced sprouting and increased dematuration in the presence of VEGF-A₁₆₅; i.e. increases in K_{EC}^v , α_0^v and λ_1^v , respectively. Given that significant changes in expression happen on relatively short time-scales (< 4 hours) [S18], to simplify our model, we assume that the upregulation of VEGFR-2 expression (and thus modulation of parameter values) and the production of VEGF-A₁₆₅ are instantaneous. In particular, we suppose that VEGFR-2 expression is upregulated according to:

$$\Lambda(f) = \Lambda_0 \left(1 + \frac{s f}{f + f_{\frac{1}{2}}^f} \right), \quad (\text{S8})$$

where s determines the maximal fold-increase in VEGFR-2 expression levels and Λ_0 is the level of VEGFR-2 expression in the absence of bFGF. In particular, here, we assume that the number of VEGFR-2 molecules per EC increases linearly with the fraction of bound FGFR-1 receptors. In the presence of bFGF, then, K_{EC}^v , α_0^v and λ_1^v , are modified w.r.t. their definitions above, (S3)-(S6), as follows:

$$K_{EC}^v \mapsto K_{EC}^v \frac{\Lambda(f)}{\Lambda_0}, \quad (\text{S9})$$

$$\alpha_0^v \mapsto \alpha_0^v \frac{\Lambda(f)}{\Lambda_0}, \quad (\text{S10})$$

$$\lambda_1^v \mapsto \lambda_1^v \frac{\Lambda(f)}{\Lambda_0}. \quad (\text{S11})$$

To account for bFGF-induced VEGF-A₁₆₅ production by ECs, we include an additional source term in the VEGF-A₁₆₅ equation, in which ECs release VEGF-A₁₆₅ at a rate proportional to the bound fraction of FGFR-1 molecules.

Having now accounted for VEGF-A₁₆₅/bFGF crosstalk, our model equations become:

$$\frac{\partial m}{\partial t} = - \left[\overbrace{\left(1 + \frac{sf}{f + f_{\frac{1}{2}}^f} \right)}^{\substack{\uparrow \text{VEGFR-2} \rightarrow \uparrow \text{VEGF-A}_{165} \\ \text{induced dematuration}}} \left(\frac{\lambda_1^v v}{v + v_{\frac{1}{2}}} \right) + \left(\frac{\lambda_1^f f}{f + f_{\frac{1}{2}}^f} \right) \right] m, \quad (\text{S12})$$

$$\begin{aligned} \frac{\partial n}{\partial t} &= \frac{\partial}{\partial x} \left(\mu \frac{\partial n}{\partial x} - \chi_f n \frac{\partial f}{\partial x} - \chi_v n \frac{\partial v}{\partial x} \right) \\ &\quad + \overbrace{\alpha_0^v \left(1 + \frac{sf}{f + f_{\frac{1}{2}}^f} \right) \left(\frac{v}{v + v_{\frac{1}{2}}} \right)}^{\substack{\uparrow \text{VEGFR-2} \rightarrow \uparrow \text{VEGF-A}_{165} \\ \text{induced sprouting}}} \rho + \alpha_0^f \left(\frac{f}{f + f_{\frac{1}{2}}^f} \right) \rho \\ &\quad - \beta_1 n (\rho + m) - 2 \beta_2 n^2 - \gamma n \left(\frac{v_{\frac{1}{2}}}{v + v_{\frac{1}{2}}} \right) \left(\frac{f_{\frac{1}{2}}^f}{f + f_{\frac{1}{2}}^f} \right), \end{aligned} \quad (\text{S13})$$

$$\begin{aligned} \frac{\partial \rho}{\partial t} &= \kappa \left| \mu \frac{\partial n}{\partial x} - \chi_f n \frac{\partial f}{\partial x} - \chi_v n \frac{\partial v}{\partial x} \right| - \gamma \rho \left(\frac{v_{\frac{1}{2}}}{v + v_{\frac{1}{2}}} \right) \left(\frac{f_{\frac{1}{2}}^f}{f + f_{\frac{1}{2}}^f} \right) \\ &\quad + \left[\left(1 + \frac{sf}{f + f_{\frac{1}{2}}^f} \right) \left(\frac{\lambda_1^v v}{v + v_{\frac{1}{2}}} \right) + \left(\frac{\lambda_1^f f}{f + f_{\frac{1}{2}}^f} \right) \right] m, \end{aligned} \quad (\text{S14})$$

$$\frac{\partial f}{\partial t} = D_f \frac{\partial^2 f}{\partial x^2} - \lambda_f v - 2 \pi \bar{R} P_f (\rho + m) f - K_{EC}^f (\rho + m) \left(\frac{f}{f + f_{\frac{1}{2}}^f} \right), \quad (\text{S15})$$

$$\frac{\partial v}{\partial t} = D_v \frac{\partial^2 v}{\partial x^2} - \lambda_v v - 2 \pi \bar{R} P_v (\rho + m) v \quad (\text{S16})$$

$$\begin{aligned} &\quad - K_{EC} \overbrace{\left(1 + \frac{sf}{f + f_{\frac{1}{2}}^f} \right) \left(\frac{v}{v + v_{\frac{1}{2}}} \right)}^{\substack{\uparrow \text{VEGFR-2} \rightarrow \uparrow \text{binding} \\ \text{of VEGF-A}_{165}}} (\rho + m) + \underbrace{\phi (\rho + m) \left(\frac{f}{f + f_{\frac{1}{2}}^f} \right)}_{\substack{\text{bFGF stimulates ECs to} \\ \text{produce VEGF-A}_{165}}}, \end{aligned}$$

Terms highlighted in red are those associated with VEGF-A₁₆₅/bFGF crosstalk. ϕ is the maximum rate of increase in VEGF-A₁₆₅ concentration due to EC exposure to bFGF.

2.7 Initial and boundary conditions

In order to close our model, comprising Equations S12-S16, it remains to prescribe appropriate boundary and initial conditions. The model is formulated on a one-dimensional Cartesian domain, $0 \leq x \leq L$, with VEGF-A₁₆₅- and bFGF-containing pellets located at $x = L$ and limbal vessels (that border the cornea) at $x = 0$. Initially, the interior of the model domain is assumed to be devoid of vessels and of VEGF-A₁₆₅ and bFGF. The initial distribution of vessels is described via a normal distribution of mature vessels, centred on $x = 0$, so that initially, inside the model domain, we have:

$$m(x, 0) = m_L \exp\left[-\frac{x^2}{2\sigma^2}\right], \quad n(x, 0) = 0, \quad \rho(x, 0) = 0, \quad v(x, 0) = 0, \quad f(x, 0) = 0,$$

where m_L is the maximal vessel density at the limbus initially and σ describes the initial spread of vascular density.

We assume that sprout tips are unable to penetrate the pellet or the limbus and, hence, impose no flux boundary conditions at $x = 0$ and $x = L$. Meanwhile, VEGF-A₁₆₅ is removed from the model domain at $x = 0$ via the limbal vasculature, the flux being proportional to the difference in concentrations of VEGF-A₁₆₅ inside the cornea, $v(0, t)$, and in the blood. The influx of VEGF-A₁₆₅ from the pellet at $x = L$ is assumed proportional to the difference in concentrations of VEGF-A₁₆₅ inside the cornea, $v(L, t)$, and inside the pellet. Similar assumptions are made regarding the behaviour of bFGF on the model boundaries. Thus, we have:

$$\left. \begin{aligned} \mu \frac{\partial n}{\partial x} - \chi_v n \frac{\partial v}{\partial x} - \chi_f n \frac{\partial f}{\partial x} = 0, \quad -D_f \frac{df}{dx} = -P_f f, \\ -D_v \frac{dv}{dx} = -P_v v, \end{aligned} \right\} x = 0, \quad (\text{S17})$$

$$\left. \begin{aligned} \mu \frac{\partial n}{\partial x} - \chi_v n \frac{\partial v}{\partial x} - \chi_f n \frac{\partial f}{\partial x} = 0, \quad -D_f \frac{df}{dx} = -k_p^f ([F_f] - f), \\ -D_v \frac{dv}{dx} = -k_p^v ([V_f] - v), \end{aligned} \right\} x = L, \quad (\text{S18})$$

Here, k_p^v and k_p^f are effective permeability constants, quantifying the rate of transfer of VEGF-A₁₆₅ and bFGF, respectively, across the cornea-pellet boundary. The PDEs (S12) and (S14) contain no spatial derivatives in m and ρ , respectively, and require no boundary conditions. The submodel which controls the evolution of the concentration of unbound angiogenic factors inside the pellet(s), $[V_f](t)$ and $[F_f](t)$, is detailed in the following section.

2.8 Controlled release of angiogenic factors submodel

In the following, we describe the controlled release submodel within the context of VEGF-A₁₆₅. The controlled release model used for bFGF follows trivially. We assume that the concentration of VEGF-A₁₆₅ in the pellet is spatially uniform and that VEGF-A₁₆₅ binds reversibly to components

of the pellet so that



where $[V_f]$ and $[V_b]$ are the concentrations of free and bound VEGF-A₁₆₅ in the pellet, respectively, and $[B]$ is the concentration of free binding sites in the pellet. $[V_T]$, the combined concentration of bound and unbound VEGF-A₁₆₅ is given by $[V_f] + [V_b]$. While bound VEGF-A₁₆₅ is assumed not to decay, unbound VEGF-A₁₆₅ in the pellet decays at a constant rate of λ_p^v . This accounts for the fact that binding to constituents of a pellet, such as sucralfate, may have a stabilising effect on VEGF-A₁₆₅ or bFGF. Unbound VEGF-A₁₆₅ also diffuses across the cornea-pellet boundary. The molar flux passing through this boundary is given by $k_p^v ([V_f] - v(L, t))$, as in (S18). We further assume that the concentration of VEGF-A₁₆₅ at all points immediately outside the pellet are equal so that the total number of moles of VEGF-A₁₆₅ lost from the pellet through the boundary per unit time is given by $\sigma_p k_p^v ([V_f] - v(L, t))$, where σ_p is the surface area of the pellet. Combining these assumptions, we suppose that the dynamics of VEGF-A₁₆₅ inside the pellet obeys the following equations:

$$\frac{d[B]}{dt} = -k_{\text{on}} [V_f] [B] + k_{\text{off}} [V_b], \quad (\text{S20})$$

$$\frac{d[V_b]}{dt} = k_{\text{on}} [V_f] [B] - k_{\text{off}} [V_b], \quad (\text{S21})$$

$$\frac{d[V_f]}{dt} = -k_{\text{on}} [V_f] [B] + k_{\text{off}} [V_b] - \lambda_p^v [V_f] - \frac{\sigma_p k_p^v}{\Omega_p} ([V_f] - v(L, t)), \quad (\text{S22})$$

$$\frac{d[V_T]}{dt} = -\lambda_p^v [V_f] - \frac{\sigma_p k_p^v}{\Omega_p} ([V_f] - v(L, t)), \quad (\text{S23})$$

where we denote the volume of the pellet by Ω_p . The total concentration of binding sites, $[B_0]$, remains constant so that $[B_0] = [B] + [V_b]$. Following [S19], we assume that reactions (S19) occur on time-scales that are much faster than those associated with decay and release of VEGF-A₁₆₅ from the pellet so that

$$k_{\text{on}} [V_f] [B] \approx k_{\text{off}} [V_b]. \quad (\text{S24})$$

Combining this assumption with the definition $[V_T] = [V_f] + [V_b]$ and further assuming that $[V_b] \ll [B]$, i.e. $[B] \approx [B_0]$, for all time, we find that

$$[V_T] = [V_f] \underbrace{\left(1 + \frac{k_{\text{on}}}{k_{\text{off}}} [B_0]\right)}_{\theta_v}. \quad (\text{S25})$$

Here, we have defined the binding constant, $\theta_v = \left(1 + \frac{k_{\text{on}}}{k_{\text{off}}} [B_0]\right)$, as in [S19].

Using (S25) to eliminate $[V_f]$ from (S23), we arrive at the following equation for $[V_T]$:

$$\frac{d[V_T]}{dt} = -\lambda_p^v \frac{[V_T]}{\theta_v} - \frac{\sigma_p k_p^v}{\Omega_p} \left(\frac{[V_T]}{\theta_v} - v(L, t) \right). \quad (\text{S26})$$

Furthermore, the boundary conditions for VEGF-A₁₆₅ in (S18) may now be rephrased in terms of

$[V_T]$:

$$-D_v \frac{\partial v}{\partial x}(L, t) = -k_p^v \left(\frac{[V_T]}{\theta_v} - v(L, t) \right). \quad (\text{S27})$$

The resulting model allows us to investigate the effects of altering the release dynamics of VEGF-A₁₆₅ from a pellet using physically motivated parameters. Additionally, we can prescribe the amount of VEGF-A₁₆₅ released into the cornea over the duration of a simulation. We denote the initial concentration of VEGF-A₁₆₅ in the pellet by $[V_T]_{init}$ so that

$$[V_T](0) = [V_T]_{init}. \quad (\text{S28})$$

2.9 Nondimensionalisation

We recast the model, (S12)-(S16), in terms of dimensionless variables. Adopting asterisk notation to denote dimensionless variables, we rescale distance with the approximate pellet-limbus distance, \hat{L} , and time with $\tau = \frac{\hat{L}^2}{D_v}$, so that

$$x^* = \frac{x}{\hat{L}} \quad \text{and} \quad t^* = \frac{t}{\tau}. \quad (\text{S29})$$

We rescale the dependent variables as

$$n^* = \frac{n}{n_0}, \quad \rho^* = \frac{\rho}{\rho_0}, \quad m^* = \frac{m}{\rho_0}, \quad v^* = \frac{v}{V_0}, \quad [V_T]^* = \frac{[V_T]}{V_0}, \quad f^* = \frac{f}{F_0} \quad \text{and} \quad [F_T]^* = \frac{[F_T]}{F_0} \quad (\text{S30})$$

and introduce the following dimensionless parameters:

$$D_v^* = 1, \quad L^* = \frac{L}{\hat{L}}, \quad m_L^* = \left(\frac{m_L}{\rho_0} \right), \quad [V_T]^*_{init} = \left(\frac{[V_T]_{init}}{V_0} \right), \quad [F_T]^*_{init} = \left(\frac{[F_T]_{init}}{F_0} \right), \quad \sigma^* = \left(\frac{\sigma}{\hat{L}} \right),$$

$$D_f^* = \left(\frac{D_f}{D_v} \right), \quad P_v^* = \left(\frac{P_v \tau}{\hat{L}} \right), \quad P_f^* = \left(\frac{P_f \tau}{\hat{L}} \right), \quad \mu^* = \left(\frac{\mu}{D_v} \right), \quad \chi_v^* = \left(\frac{\chi_v V_0}{D_v} \right), \quad \chi_f^* = \left(\frac{\chi_f F_0}{D_v} \right),$$

$$k_p^{v*} = \left(\frac{\tau k_p^v}{\hat{L}} \right), \quad k_p^{f*} = \left(\frac{\tau k_p^f}{\hat{L}} \right), \quad \sigma_p = \left(\frac{\sigma_p}{\hat{L}^2} \right), \quad \Omega_p^* = \left(\frac{\Omega_p}{\hat{L}^3} \right), \quad \lambda_p^{v*} = (\lambda_p^v \tau), \quad \theta_v^* = \theta_v,$$

$$\lambda_p^{f*} = (\lambda_p^f \tau), \quad \theta_f^* = \theta_f, \quad \lambda_1^{v*} = (\lambda_1^v \tau), \quad \lambda_1^{f*} = (\lambda_1^f \tau), \quad \alpha_0^{v*} = \left(\frac{\alpha_0^v \tau \rho_0}{n_0} \right), \quad \alpha_0^{f*} = \left(\frac{\alpha_0^f \tau \rho_0}{n_0} \right),$$

$$\beta_1^* = (\beta_1 \rho_0 \tau), \quad \beta_2^* = (\beta_2 n_0 \tau), \quad \gamma^* = (\gamma \tau), \quad \kappa^* = \left(\frac{\kappa n_0 \hat{L}}{\rho_0} \right), \quad v_{\frac{1}{2}}^* = \left(\frac{v_{\frac{1}{2}}}{V_0} \right),$$

$$f_{\frac{1}{2}}^{FGFR*} = \left(\frac{f_{\frac{1}{2}}^f}{F_0} \right), \quad \bar{R}^* = (\bar{R} \rho_0 L), \quad \lambda_v^* = (\lambda_v \tau), \quad \lambda_f^* = (\lambda_f \tau),$$

$$K_{EC}^{v*} = \left(\frac{K_{EC}^v \tau \rho_0}{V_0} \right), \quad K_{EC}^{f*} = \left(\frac{K_{EC}^f \tau \rho_0}{F_0} \right), \quad \phi^* = \left(\frac{\phi \tau \rho_0}{V_0} \right) \quad \text{and} \quad s^* = s.$$

Substituting with (S29) and (S30) in (S12)-(S16), and exploiting the dimensionless parameters

defined above, we obtain the following system of dimensionless equations (asterisks are omitted for clarity of presentation):

$$\frac{\partial m}{\partial t} = - \left[\left(1 + \frac{sf}{f + f_{\frac{1}{2}}^f} \right) \left(\frac{\lambda_1^v v}{v + v_{\frac{1}{2}}} \right) + \left(\frac{\lambda_1^f f}{f + f_{\frac{1}{2}}^f} \right) \right] m, \quad (\text{S31})$$

$$\begin{aligned} \frac{\partial n}{\partial t} &= \frac{\partial}{\partial x} \left(\mu \frac{\partial n}{\partial x} - \chi_f n \frac{\partial f}{\partial x} - \chi_v n \frac{\partial v}{\partial x} \right) \\ &+ \alpha_0^v \left(1 + \frac{sf}{f + f_{\frac{1}{2}}^f} \right) \left(\frac{v}{v + v_{\frac{1}{2}}} \right) \rho + \alpha_0^f \left(\frac{f}{f + f_{\frac{1}{2}}^f} \right) \rho \\ &- \beta_1 n (\rho + m) - 2 \beta_2 n^2 - \gamma n \left(\frac{v_{\frac{1}{2}}}{v + v_{\frac{1}{2}}} \right) \left(\frac{f_{\frac{1}{2}}^f}{f + f_{\frac{1}{2}}^f} \right), \end{aligned} \quad (\text{S32})$$

$$\begin{aligned} \frac{\partial \rho}{\partial t} &= \kappa \left| \mu \frac{\partial n}{\partial x} - \chi_f n \frac{\partial f}{\partial x} - \chi_v n \frac{\partial v}{\partial x} \right| - \gamma \rho \left(\frac{v_{\frac{1}{2}}}{v + v_{\frac{1}{2}}} \right) \left(\frac{f_{\frac{1}{2}}^f}{f + f_{\frac{1}{2}}^f} \right) \\ &+ \left[\left(1 + \frac{sf}{f + f_{\frac{1}{2}}^f} \right) \left(\frac{\lambda_1^v v}{v + v_{\frac{1}{2}}} \right) + \left(\frac{\lambda_1^f f}{f + f_{\frac{1}{2}}^f} \right) \right] m, \end{aligned} \quad (\text{S33})$$

$$\frac{\partial f}{\partial t} = D_f \frac{\partial^2 f}{\partial x^2} - \lambda_f v - 2 \pi \bar{R} P_f (\rho + m) f - K_{EC}^f (\rho + m) \left(\frac{f}{f + f_{\frac{1}{2}}^f} \right), \quad (\text{S34})$$

$$\begin{aligned} \frac{\partial v}{\partial t} &= D_v \frac{\partial^2 v}{\partial x^2} - \lambda_v v - 2 \pi \bar{R} P_v (\rho + m) v \\ &- K_{EC}^v \left(1 + \frac{sf}{f + f_{\frac{1}{2}}^f} \right) \left(\frac{v}{v + v_{\frac{1}{2}}} \right) (\rho + m) + \phi (\rho + m) \left(\frac{f}{f + f_{\frac{1}{2}}^f} \right), \end{aligned} \quad (\text{S35})$$

$$\frac{d[F_T]}{dt} = - \frac{\lambda_p^f}{\theta_f} [V_T] - \frac{\sigma_p k_p^f}{\Omega_p} \left(\frac{[F_T]}{\theta_f} - f(L, t) \right), \quad (\text{S36})$$

$$\frac{d[V_T]}{dt} = - \frac{\lambda_p^v}{\theta_v} [V_T] - \frac{\sigma_p k_p^v}{\Omega_p} \left(\frac{[V_T]}{\theta_v} - v(L, t) \right). \quad (\text{S37})$$

Once more, these equations are subject to the boundary conditions

$$\left. \begin{aligned} \mu \frac{\partial n}{\partial x} - \chi_v n \frac{\partial v}{\partial x} - \chi_f n \frac{\partial f}{\partial x} &= 0, & -D_f \frac{df}{dx} &= -P_f f, \\ -D_v \frac{dv}{dx} &= -P_v v, \end{aligned} \right\} x = 0, \quad (\text{S38})$$

$$\left. \begin{aligned} \mu \frac{\partial n}{\partial x} - \chi_v n \frac{\partial v}{\partial x} - \chi_f n \frac{\partial f}{\partial x} &= 0, & -D_f \frac{df}{dx} &= -k_p^f \left(\frac{[F_T]}{\theta_f} - f \right), \\ -D_v \frac{dv}{dx} &= -k_p^v \left(\frac{[V_T]}{\theta_v} - v \right), \end{aligned} \right\} x = L, \quad (\text{S39})$$

and to the initial conditions

$$\begin{aligned} m(x, 0) &= m_L \exp \left[-\frac{x^2}{2\sigma^2} \right], & n(x, 0) &= 0, & \rho(x, 0) &= 0, & v(x, 0) &= 0, & f(x, 0) &= 0, \\ [F_T](0) &= [F_T]_{init}, & [V_T](0) &= [V_T]_{init}. \end{aligned} \quad (\text{S40})$$

3 Parameter value estimation

In this section we discuss our choice of default parameter values, beginning with the scalings for time, distance and the dependent variables. Following this, we discuss the values of model parameters. For model parameterisation we focussed on two *in vivo* scenarios, as noted in the main text:

S2. VEGF-A₁₆₅ experiments: $[V_T]_{init}$ at its default value, $[F_T]_{init} = 0$;

S3. bFGF experiments: $[V_T]_{init} = 0$, $[F_T]_{init}$ at its default value.

Setting $[F_T]_{init} = 0$ (S2) allows us to fix parameters associated with VEGF-A₁₆₅-induced angiogenesis. With the VEGF-A₁₆₅ submodel parameters fixed we then consider the second case: $[V_T]_{init} = 0$ (S3).

Due to issues regarding parameter identifiability and the resulting ill-posed nature of the parameter fitting problem we do not attempt formally to fit the model parameters to the data. Instead, we base our parameter estimates on published data wherever possible; where appropriate experimental data are not available, we use physical arguments and previous modelling efforts to derive approximate values. Where neither of these options are viable, parameter values are manually tuned such that model simulation results are in good quantitative agreement with the data extracted from experimental images (Figure 5 in the main manuscript). By employing such a manual tuning approach we show that our models are able to capture quantitatively the available experimental data when model parameters are chosen within an acceptable physical range. Fitting our models to the data by solving the optimisation problem would, at best, not yield parameter values which are more useful than those which we have arrived at through manual tuning, and, at worst, be misleading.

Table S2 summarises the values of the scaling factors for the independent and dependent variables used to nondimensionalise our model, while Tables S3-S5 summarise the default model parameter values and detail sources, where available.

Scaling parameters

Since pellets are placed at a distance of approximately 1 mm from the limbal vessels, this represents a natural choice for our length scale, \hat{L} . The time taken for VEGF-A₁₆₅ to diffuse a root mean squared distance of \hat{L} in one dimension is given by $\frac{\hat{L}^2}{2D_v}$. However, following Byrne and Chaplain [S13], to simplify our nondimensionalisation we use a time-scale of $\tau = \frac{\hat{L}^2}{D_v}$. Vessel density is scaled with the initial density of mature vessels at the limbus, m_L (see Equation S40). The value for m_L is estimated by assuming that the limbal vessel density represents a single vessel running perpendicular to the x -axis. If Δ_z is the thickness of the cornea, Δ_y is the length along the limbus in which we are interested and ϕ is the tortuosity of the limbal vasculature then we can equate the total length of limbal vessels using

$$\phi \Delta_y = \Delta_y \Delta_z \int_{-\infty}^{\infty} m_L \exp\left(\frac{-x^2}{2\sigma^2}\right) dx. \quad (\text{S41})$$

Solving and rearranging this equation, we find $m_L = \frac{\phi}{\sqrt{2\pi}\sigma\Delta_z}$. Assuming a value of 20 μm for σ , the initial width of the vessel density distribution, and by approximating $\phi = 1.1$ and the thickness of the cornea, $\Delta_z = 100 \mu\text{m}$ [S5, S6], we calculate $m_L \approx 2 \times 10^8 \text{ m of vessel m}^{-3}$. Our estimate here is also in good agreement with the data extracted from experimental images (Section 1). Initial numerical simulations suggested a convenient scaling factor for VEGF-A₁₆₅, V_0 , to be of the same order of magnitude as $v_{\frac{1}{2}}$, the concentration of VEGF-A₁₆₅ at which EC activation is half-maximal, which corresponds to the EC50 for VEGFR-2 activation by VEGF-A₁₆₅. Akesson *et al.* [S20] estimate $v_{\frac{1}{2}} = 650 \text{ pM}$, which is within the range of dissociation constants for VEGF-A₁₆₅ binding to VEGFR-2 receptors on human colonic ECs reported in Wang *et al.* [S21]: 600–700 pM . We use the value for $v_{\frac{1}{2}}$ estimated by Akesson *et al.* [S20]. For our scaling factor, we fix $V_0 = 5 v_{\frac{1}{2}} = 3.25 \times 10^{-9} M$, since this ensures that the maximum scaled value of VEGF-A₁₆₅ inside the cornea in default simulations is $\mathcal{O}(1)$. The scaling factors for the sprout tip density, $n_0 = 1 \times 10^{12} \text{ tips m}^{-3}$, and bFGF, $F_0 = 1 \times 10^{-9} M$ are chosen such that the scaled tip density and bFGF concentration are $\mathcal{O}(1)$ in default simulations.

VEGF-A₁₆₅ submodel parameterisation

Equation (S31), governing the mature vessel length density, contains one additional parameter associated with VEGF-A₁₆₅-induced angiogenesis, λ_1^v (the default value of $v_{\frac{1}{2}}$ was discussed above). λ_1^v is difficult to estimate because the term describing dematuration captures many complex biochemical interactions and cellular processes in a simple way. Thus, we estimate a value for λ_1^v by taking inspiration from a complex biochemical model. Zheng *et al.* [S9] consider a model of vessel maturation and dematuration which included VEGF-A, Ang-1, Ang-2, ECs, pericytes, PDGF-B and a number of corresponding cell-surface receptors. In their model, the activation rate of quiescent ECs in high Ang-2 conditions is given by $1.25 \times 10^2 \text{ per } \mu\text{M bound Ang-2 per hour}$. Drawing on evidence from the literature [S22, S23, S24], Zheng *et al.* use $10^{-3} \mu\text{M}$ as the reference concentration of Angiopoetins and $10^{-3} \mu\text{M}$ as the reference concentration of Tie-2 receptors. Thus, for our model of maturation to be consistent with that of Zheng *et al.*, we expect our maximal rate of dematuration, λ_1^v to take on a value of $\sim 0.1 \text{ h}^{-1}$. For our simulations, we choose a default value of $\lambda_1^v = 0.156 \text{ h}^{-1}$.

The parameter μ is the random motility coefficient for tip cells. A number of experiments have been performed which allow us to estimate the random motility of individual ECs. For example, by

Scaling parameter	Description	Value [units]
\hat{L}	Length scale. Approximate distance between limbal vessels and pellet.	0.001 [m]
τ	Time scale. Time for VEGF-A ₁₆₅ to diffuse from the pellet to limbal vessels.	5.13 [h]
V_0	Reference value for VEGF-A ₁₆₅ concentration.	3.25×10^{-9} [M]
F_0	Reference value for bFGF concentration.	1×10^{-9} [M]
n_0	Reference value for sprout tip density.	1×10^{12} [tips m ⁻³]
ρ_0	Reference value for (mature and immature) vessel length density.	2×10^8 [m of vessels m ⁻³]

Table S2: Scaling parameters for the model, (S31)-(S40)

fitting mathematical models to experiments involving epidermal wound healing *in vivo*, Sherratt and Murray [S25] estimate $\mu = 2.46 \times 10^{-11} - 3.6 \times 10^{-9} \text{ m}^2\text{h}^{-1}$, while Stokes *et al.* [S26] estimate $\mu = 2.56 \pm 0.97 \times 10^{-9} \text{ m}^2\text{h}^{-1}$ for individual ECs *in vitro*. Meanwhile, Kouvroukoglou *et al.* [S27] study individual EC migration on different surfaces and find $\mu = 3.5 \times 10^{-10} - 1.15 \times 10^{-9} \text{ m}^2\text{h}^{-1}$. However, as noted, these studies consider individual ECs and we expect tip cells to be less motile than isolated ECs due to cell-cell interactions with trailing ECs [S28]. In their models of corneal angiogenesis, Byrne and Chaplain [S13] approximate $\mu = 10^{-3}D_v \approx 10^{-11} - 10^{-10} \text{ m}^2\text{h}^{-1}$, as does Addison-Smith [S29]. In their composite hybrid model of vascular tumour growth, Owen *et al.* [S30] use $\mu = 6 \times 10^{-11} \text{ m}^2\text{h}^{-1}$. We also find that a value of $\mu = 6 \times 10^{-11} \text{ m}^2\text{h}^{-1}$ provides a good fit to our experimental data. The parameter χ_v , the chemotaxis coefficient for tip cells, quantifies the strength of the motile response of tip cells to gradients of VEGF-A₁₆₅. Stokes *et al.* [S31] use an under-agarose assay to estimate $\chi_v = 936 \pm 270 \text{ m}^2\text{h}^{-1}\text{M}^{-1}$ for individual ECs in gradients of acidic FGF, where concentrations of acidic FGF were around 10^{-10} M. Again, we expect tip cells to be less motile than isolated ECs. Both Balling and McElwain and Byrne and Chaplain, guided by the experiments of Stokes *et al.*, estimate $\chi_v = \frac{D_v}{V_0}$ to provide results in qualitative agreement with experimental data [S32]. Whereas Addison-Smith uses a smaller value ($\chi_v = 0.125 \times \frac{D_v}{V_0}$) to provide results in qualitative agreement with an alternative set of experiments [S33]. We use $\chi_v = 1.837 \text{ m}^2\text{h}^{-1}\text{M}^{-1}$ to produce results that are consistent with our experimental data. Given our scalings, this value is similar in magnitude to that used by Addison-Smith.

The parameters α_0^v , κ , β_1 , β_2 and γ determine the rates of production and destruction of tip cells (and immature vessels) in the presence of VEGF-A₁₆₅. We estimate α_0^v by assuming that the maximal rate of tip production is limited by the doubling time of ECs. The typical doubling time of a proliferating cell is about 20 hours, corresponding to a doubling rate of $k_{double} = 0.035 \text{ h}^{-1}$. We also assume that only one in every two ECs may become a tip cell due to Delta-Notch mediated lateral inhibition [S34]. We estimate the maximal rate of tip production per unit vessel length density by further assuming that an EC covers an area of $260 \mu\text{m}^2$ [S19, S35] of a vessel wall, and that vessels are on average $10 \mu\text{m}$ in diameter (see discussion on page 18). Then, assuming that vessels can be approximated by cylinders, we estimate $\nu = 1.2 \times 10^5$ ECs per metre of vessel. Then we estimate $\alpha_0^v = 0.5 \times 0.035 \times 1.2 \times 10^5 = 2100$ tips per hour per metre of vessel. In practice, numerical simulations reveal that slightly larger values of α_0^v give results which are in better agreement with our experimental data. Thus, we choose $\alpha_0^v = 2600$ tips per hour per metre of vessel. Given that tip formation and vascular growth may occur in the absence of EC proliferation [S36], this value is still reasonable.

An order of magnitude estimate for γ , the maximal rate of vessel regression, can be obtained from results reported in Cao *et al.* [S10]. They observed complete regression of VEGF-A-induced neovasculature in cornea assay experiments within 7 days after the source of VEGF-A was removed. Consistent with their observations, we fix $\gamma = 2.27 \times 10^{-3} \text{ h}^{-1}$ since this also provides a good fit to our experimental data. Values for β_1 and β_2 , the rates of tip-to-vessel and tip-to-tip anastomosis, respectively, are difficult to estimate. We fix $\beta_1 = 0.156 \times 10^{-9} \text{ anastomosis events h}^{-1} (\text{m of vessel m}^{-3})^{-1} (\text{cells m}^{-3})^{-1} \text{ m}^{-3}$ and $\beta_2 = 1 \times 10^{-15} \text{ anastomosis events h}^{-1} (\text{cells m}^{-3})^{-2} \text{ m}^{-3}$. Note that $\frac{\beta_1^*}{\beta_2^*} \approx 30$, reflecting the fact that we expect tip-to-tip anastomosis events to be rarer than tip-to-vessel anastomosis events. κ quantifies the length of immature vessel produced in the plane perpendicular to the x -direction when a sprout tip moves in the x direction. Motion along the x -axis corresponds to $\kappa = 1$, while larger values of κ indicate increasing amounts of lateral movement. We assume that $\kappa = 3.15 \text{ metre of vessel cell}^{-1} \text{ m}^{-1}$.

The parameter D_v is the diffusion coefficient for VEGF-A₁₆₅ in the cornea. By monitoring the intensity of fluorescently labelled VEGF-A₁₆₅, Chen *et al.* [S37] estimate the diffusivity of VEGF-A₁₆₅ in Matrigel to be $2.52 \times 10^{-7} \text{ m}^2 \text{ h}^{-1}$. Meanwhile, MacGabhann[S38] and Ambrosi *et al.* [S39] propose estimates of $D_v \approx 10^{-7} \text{ m}^2 \text{ h}^{-1}$, having used the Einstein-Stokes formula. Here, we use a value of D_v similar to that given by Chen *et al.* as default: $D_v = 1.95 \times 10^{-7} \text{ m}^2 \text{ h}^{-1}$. Chen *et al.* and Serini *et al.* [S40] estimate λ_v , the natural decay constant for VEGF-A₁₆₅, to be $\lambda_v = 0.8316 \text{ h}^{-1}$ and $\lambda_v = 0.65 \text{ h}^{-1}$, respectively, in Matrigel. As a default value, we fix $\lambda_v = 0.8 \text{ h}^{-1}$.

K_{EC}^v is the maximum rate of reduction in molar VEGF-A₁₆₅ concentration per unit vessel length density due to VEGFR-2 binding. Wang *et al.* [S21] estimate the average number of VEGFR-2 receptors per cell to be approximately 230000, so that, at any time, at most $230000 / N_A = 3.82 \times 10^{-19}$ moles of VEGF-A₁₆₅ can bind to VEGFR-2 receptors on an EC (where N_A is Avogadro's number). MacGabhann and Popel [S41] estimate the instantaneous internalisation rate of VEGF-A in human umbilical vein endothelial cells (HUVECs) as 1.548 h^{-1} using data from [S42], and as 1.008 h^{-1} using data from [S21]. Thus, if VEGFR-2 receptor numbers remain constant on the surface of a cell then we expect ECs to uptake $3.82 \times 10^{-19} \times 1.008 \approx 4 \times 10^{-19} - 3.82 \times 10^{-19} \times 1.548 \approx 6 \times 10^{-19}$ moles of VEGF-A₁₆₅ maximally per hour. In practice, only a fraction of the VEGFR-2 receptors are ever present on the surface of the cell since others are being internalised and/or being recycled. However, since we are not modelling receptor kinetics directly we estimate the uptake rate of endothelial cells as $4 \times 10^{-22} \text{ moles h}^{-1} \text{ cell}^{-1} \text{ litre}^{-1} \text{ m}^3$. Then, using our estimate of 1.2×10^5 ECs per metre of vessel, as before, $K_{EC}^v = 1.2 \times 10^5 \times 4 \times 10^{-22} = 4.8 \times 10^{-17} \text{ moles h}^{-1} (\text{m of vessel})^{-1} \text{ litre}^{-1} \text{ m}^3$

Fu and Shen [S43] calculate the permeability of vessels to α -lactalbumin and albumin when exposed to 1 nM VEGF-A₁₆₅. α -lactalbumin and albumin are molecules with Stokes radii of 20.1 and 35.0 Angstroms, respectively, similar to that of VEGF-A₁₆₅ (30.2 Angstroms). They find the peak permeability of vessel walls to be $6.12 \times 10^{-4} \text{ m h}^{-1}$ for α -lactalbumin and $1.332 \times 10^{-4} \text{ m h}^{-1}$ for albumin in 1 nM VEGF-A₁₆₅ and $1.98 \times 10^{-4} \text{ m h}^{-1}$ for α -lactalbumin and $2.448 \times 10^{-5} \text{ m h}^{-1}$ for albumin when VEGF-A₁₆₅ is not applied. In their paper, Stefanini *et al.* [S44] review experimental papers pertaining to the permeability of vasculature to VEGF-A. They conclude that vascular permeability in the presence of VEGF-A is likely to lie between $1.44 \times 10^{-6} \text{ m h}^{-1}$ and $1.44 \times 10^{-3} \text{ m h}^{-1}$ and estimate P_v to be $1.44 \times 10^{-6} \text{ m h}^{-1}$ in normal tissues, where levels of VEGF-A are low. We use a default value of $P_v = 3 \times 10^{-4} \text{ m h}^{-1}$ in our simulations. In the absence of VEGF-A, Tsai *et al.* [S45] find the average diameters of *in vivo* and histological microvessels in the murine

brain to be $3.97\ \mu\text{m}$ and $4.11\ \mu\text{m}$, respectively. We expect diameters to be larger than this in the presence of VEGF-A₁₆₅. On the other hand, Peebo *et al.* [S46] measure the limbal vessel diameter in rats and find them to vary between $9 - 12\ \mu\text{m}$ on day 1 and $25 - 30\ \mu\text{m}$ at their peak diameter in an inflammatory corneal angiogenesis experiment. Thus, we fix $\bar{R} = 5\ \mu\text{m}$ for the radius of vessels.

In the absence of suitable experimental data, we assume $\theta_v = 54.4$, $k_p^v = 2.94 \times 10^{-7}\ \text{m h}^{-1}$ and $\lambda_p^v = 0.8\ \text{h}^{-1}$ since these values yield results in good agreement with our experimental data. In particular, we assume that the decay rate of free VEGF-A₁₆₅ in the pellet is the same as that in the cornea. The surface area, σ_p , and the volume, Ω_p , of the cylindrical pellets can be calculated since their height is $0.06\ \text{mm}$ and their radius $0.3\ \text{mm}$. Our default simulations involve pellets containing $300\ \text{ng}$ of VEGF-A₁₆₅, which has a molecular weight of approximately $45\ \text{kDa}$. Given the volume of the pellet, we estimate the initial molar concentration of VEGF-A₁₆₅ in the pellet to be $3.93 \times 10^{-4}\ \text{M}$.

Finally, for VEGF-A₁₆₅ experiments an estimate for the pellet-limbus distance, $L = 1.04\ \text{mm}$, was obtained from the image processing steps outlined in Section 1.

bFGF-induced angiogenesis parameterisation

Parameters associated with both VEGF-A₁₆₅- and bFGF- induced angiogenesis (Table S3) and shown to provide a good fit to data arising from VEGF-A₁₆₅ experiments (see Figure 5a in the main manuscript) were considered fixed when estimating parameters associated with bFGF-induced angiogenesis.

Other parameters associated with bFGF-induced angiogenesis which may be estimated from published data were mainly associated with bFGF transport, degradation and uptake. Bikfalvi *et al.* [S47] estimate $f_{\frac{1}{2}}^f = 42.2 \pm 3.8\ \text{pM}$. They also estimate the number of FGFR binding sites per human omental microvascular EC to be 70000 ± 6000 sites per cell. Meanwhile, Moscatelli [S48] estimate $6000 - 17000$ FGFR receptors per bovine capillary EC. Moscatelli [S48] also finds the dissociation constant of FGFR to be $\sim 20\ \text{pM}$. The internalisation rate of the bFGF/FGFR complex is $4.68\ \text{h}^{-1}$ [S49, S50]. We use the estimates given by Bikfalvi *et al.* [S47] to parameterise our model; we take $f_{\frac{1}{2}}^f = 4.22\ \text{pM}$ and assume 70000 FGFR-1 binding sites per EC. Maximally, therefore, 1.16×10^{-19} moles of bFGF can bind to FGFR receptors on ECs at any one time. Thus, assuming that the number of receptors on the surface of a cell remains constant, a cell can uptake maximally 5.4×10^{-19} moles of bFGF per hour via FGFR-1 molecules. Using our estimate of 1.2×10^5 ECs per metre of vessel, as in Section 3, we estimate initially $K_{EC}^f = 1.2 \times 10^5 \times 5.4 \times 10^{-22} = 6.48 \times 10^{-17}\ \text{moles h}^{-1} (\text{m of vessel})^{-1} \text{ litre}^{-1} \text{ m}^3$. However, in default simulations we use a value of $2.16 \times 10^{-17}\ \text{moles h}^{-1} (\text{m of vessel})^{-1} \text{ litre}^{-1} \text{ m}^3$ for K_{EC}^f since this provides a better fit to experimental data whilst still being consistent with values found in the literature.

Tong and Yuan [S19] follow Boyer and Hsu [S51], estimating the diffusion coefficient of bFGF as $D_f = 1.92 \times 10^{-7}\ \text{m}^2\text{h}^{-1}$, while Filion and Popel [S50] estimate the diffusion coefficient for bFGF to be $7.92 \times 10^{-7}\ \text{m}^2\text{h}^{-1}$ at 37°C using the Einstein-Stokes formula. For our simulations we follow Tong and Yuan [S19] and fix $D_f = 1.92 \times 10^{-7}\ \text{m}^2\text{h}^{-1}$. Westall *et al.* [S52] investigate the activity of FGF at different pH levels, finding the half-life of FGF, λ_f , to vary between a few hours and a day (or so) and Sperinde and Nugent [S53] provide an estimate for the half-life of bFGF inside the cell of $18 - 24$ hours. We fix $\lambda_f = 0.04\ \text{h}^{-1}$, corresponding to a half-life of approximately 18 hours. Fu and

Shen [S43] estimate the permeability of vessels to α -lactalbumin to be $(1.98 \pm 0.216) \times 10^{-4} \text{ m h}^{-1}$. Since α -lactalbumin has a similar Stokes' radius (20.1 Angstroms) to bFGF (14.5 Angstroms [S54]), we fix $P_f = 1 \times 10^{-4} \text{ m h}^{-1}$ for the permeability of vessels to bFGF.

Default simulations mimic experiments involving cylindrical pellets of radius 0.3 mm and thickness 0.06 mm which contain 15 ng bFGF (18 kDa). Thus, we estimate the initial molar concentration of bFGF in the pellet to be $[F_T]_{init} = 4.92 \times 10^{-5} \text{ M}$. In the absence of suitable experimental data, we assume $\theta_f = 50$, $k_p^f = 3.95 \times 10^{-7} \text{ m h}^{-1}$ and $\lambda_p^f = \lambda_f = 0.04 \text{ h}^{-1}$ since these values yield results in good agreement with our experimental data (Figure 5b in the main manuscript).

Parameters which remain to be estimated are λ_1^f , χ_f , α_0^f , s and ϕ . Pepper and Mandriota [S18] report a fold-increase in total protein levels of VEGFR-2 when ECs are exposed to bFGF ($5.3 \times 10^{-4} \text{ M} \gg f_{\frac{1}{2}}^f$) of between 2 and 3.5. Thus, here, we set $s = 1$, assuming a maximal fold-increase of 2. In the absence of appropriate experimental data, we set ϕ , the maximal rate of increase in VEGF-A₁₆₅ concentration per unit vessel length density, to $1.2 \times 10^{-17} \text{ moles h}^{-1} (\text{m of vessel})^{-1} \text{ litre}^{-1} \text{ m}^3$, which is the same order of magnitude as K_{EC}^v , the maximum rate of VEGF-A₁₆₅ removal due to its binding with VEGFR-2 on ECs.

Estimates for λ_1^f , χ_f and α_0^f were first obtained by assuming no VEGF-A₁₆₅/bFGF crosstalk, that is $s = \phi = 0$. In this case, bFGF-induced angiogenesis is decoupled from the VEGF-A₁₆₅ submodel, and $\lambda_1^f = 0.0343 \text{ h}^{-1}$, $\chi_f = 3.264 \text{ m}^2 \text{ h}^{-1} \text{ M}^{-1}$, and $\alpha_0^f = 715 \text{ tips h}^{-1} \text{ per m of vessel}$ were found to provide a good fit to experimental data. When default values of s and ϕ are used λ_1^f , χ_f and α_0^f must be modulated to ensure that model results remain commensurate with the experimental data (Figure 5b in the main manuscript). In particular, in our model, in the absence of a VEGF-A₁₆₅ pellet, VEGF-A₁₆₅ is still produced by ECs, primarily around the vascular wavefront which is exposed to significant levels of bFGF. Initially, this leads to increased dematuration. To ensure that model results remain commensurate with the experimental data this additional dematuration due to VEGF-A₁₆₅ must be balanced by a reduction in the rate of dematuration due to bFGF. Thus, the value of λ_1^f is lower than estimated for the case where $s = \phi = 0$. Similarly, VEGF-A₁₆₅ production at the front causes increased sprouting, which must be compensated for with a reduction in the sprouting rate due to bFGF, α_0^f . The VEGF-A₁₆₅ produced by ECs around the vascular front diffuses, decays and is taken up by the vasculature, producing a small negative VEGF-A₁₆₅ gradient moving from the front to the pellet (and from the front to the limbus). Thus, sprout tip closest to the leading edge experience a chemotactic force directed away from the pellet, reducing the speed of migration of the vascular front. To compensate for this χ_f is increased w.r.t. the estimated value when $s = \phi = 0$. The default values for λ_1^f , χ_f and α_0^f when default values for s and ϕ are used are presented in Table S5.

For bFGF experiments an estimate for the pellet-limbus distance, $L = 1.12 \text{ mm}$, was obtained from the image processing steps outlined in Section 1. A value of $L = 1.12 \text{ mm}$ is also assumed for experiments in which VEGF-A₁₆₅ and bFGF are administered in combination.

3.1 Parameterising alternate model variants

To determine the impact of VEGF-A₁₆₅/bFGF crosstalk on the angiogenic response of the corneal vasculature we performed *in silico* knock-out experiments, in which different crosstalk terms were eliminated. The four model variants we consider are summarised in Table 1 in the main manuscript.

Parameter	Description	Default value and units	Non-dimensional value	Sources
σ	Initial width of limbal vessel density distribution.	20×10^{-6} [m]	0.02	-
m_L	Maximum density of mature vessel length density at the limbus initially.	2×10^8 [m of vessel m^{-3}]	1	-
μ	Random motility coefficient for sprout tips.	6×10^{-11} [$\text{m}^2 \text{h}^{-1}$]	3.08×10^{-4}	[S13, S25, S26, S27, S29, S30].
β_1	Rate of tip-to-vessel anastomosis per unit vessel length density per unit tip density per unit volume.	0.156×10^{-9} [anastomosis events $\text{h}^{-1} \text{m}^{-3}$ (m of vessels m^{-3}) $^{-1}$ (cells m^{-3}) $^{-1}$]	0.16	-
β_2	Rate of tip-to-tip anastomosis per unit tip density squared per unit volume.	1.03×10^{-15} [anastomosis events $\text{h}^{-1} \text{m}^{-3}$ (cells m^{-3}) $^{-2}$]	0.0053	-
γ	Maximal rate of regression of ECs (vessels).	2.27×10^{-3} [h^{-1}]	1.17×10^{-2}	[S10]
κ	Parameter quantifying the length of vessel left behind in a unit volume after a sprout tip moves out of that unit volume.	3.15 [m of vessel cells $^{-1} \text{m}^{-1}$]	15.76	-
s	Maximal fold increase in VEGFR-2 receptors induced by bFGF binding to FGFR-1.	1	1	[S18]
ϕ	Maximal rate of increase in VEGF-A ₁₆₅ concentration due to bFGF binding to FGFR-1 per unit EC density.	1.2×10^{-17} [moles of VEGF ₁₆₅ h^{-1} (m of vessel) $^{-1}$ litre $^{-1} \text{m}^3$]	3.79	-
\bar{R}	Average radius of vessels in cornea.	5×10^{-6} [m]	1	[S45, S46]
Ω_p	Volume of pellet.	1.7×10^{-11} [m^3]	1.7×10^{-2}	Hoffmann-La Roche, Penzberg.
σ_p	Surface area of pellet.	6.79×10^{-7} [m^2]	0.679	Hoffmann-La Roche, Penzberg.

Table S3: List of parameters which span both submodels of VEGF-A₁₆₅- and bFGF-induced angiogenesis, (S31)-(S40).

Simulations in which bFGF-induced VEGF-A₁₆₅ production is neglected correspond to parameterisations where $\phi = 0$. For those in which bFGF-induced VEGFR-2 upregulation is neglected we fix $s = 0$. Each variant is parameterised so that it is quantitatively consistent with the data from bFGF-induced angiogenesis experiments (Figure 5b in the main manuscript). Modifying λ_1^f , α_0^f and χ_f was sufficient to provide good fits to the experimental data (all other parameter values were held fixed at the values given in Tables S3-S5). For each variant, the fold changes in these parameter values (w.r.t. those stated in Table S5) are shown in Table S6.

Parameter	Description	Default value and units	Non-dimensional value	Sources
λ_1^v	Maximal rate of vessel dematuration.	0.156 [h ⁻¹]	0.8	[S9]
χ_v	Chemotaxis coefficient for sprout tips to VEGF-A ₁₆₅ .	1.837 [m ² h ⁻¹ M ⁻¹]	0.0306	[S12, S13, S29, S31].
α_0^v	Maximum rate of VEGF-A-induced tip production per length of vessel.	2600 [tips h ⁻¹ (m of vessel) ⁻¹]	2.668	-
D_v	Diffusion constant for VEGF-A ₁₆₅ in cornea.	1.95×10^{-7} [m ² h ⁻¹]	1	[S37, S38, S39].
λ_v	Natural decay constant of VEGF-A ₁₆₅ .	0.8 [h ⁻¹]	4.105	[S37, S40].
K_{EC}^v	Maximum rate of reduction in molar VEGF – A ₁₆₅ concentration per unit EC density due to VEGFR-2 binding.	4.8×10^{-17} [moles of VEGF ₁₆₅ h ⁻¹ (m of vessel) ⁻¹ litre ⁻¹ m ³]	15.16	[S21, S41, S42].
$v_{\frac{1}{2}}$	Concentration of VEGF-A ₁₆₅ at which VEGFR-2 receptors are half occupied.	6.5×10^{-10} [M]	0.02	[S20, S21]
P_v	Permeability of corneal vasculature to VEGF.	3×10^{-4} [m h ⁻¹]	1.54	[S43, S44].
θ_v	Binding constant.	54.4	54.4	-
k_p^v	Effective permeability of the cornea-pellet boundary.	2.94×10^{-7} [m h ⁻¹]	1.51×10^{-3}	-
λ_p^v	Natural decay constant of VEGF-A ₁₆₅ in the pellet.	0.8 [h ⁻¹]	4.105	Assume $\lambda_p = \lambda_v$.
$[V_T]_{init}$	Initial concentration of VEGF-A ₁₆₅ in pellet.	3.93×10^{-4} [M]	1.2092×10^5	Hoffmann-La Roche, Penzberg.

Table S4: List of parameters associated with VEGF-A₁₆₅-induced angiogenesis submodel only.

4 Mathematical model implementation

Equations (S31)-(S40) were solved using the method of lines. The equations were first discretised in space using central (finite) difference approximations. This reduces the model to a system of ODEs in time which we solved using MATLAB’s inbuilt routine ode15s, a variable time-step, variable-order solver for stiff problems [S55]. We set the maximum order of the solver to one to ensure numerical stability. MATLAB code for reproducing the results from model simulations is available at [S7].

5 Parameter sensitivity analysis

We may use our computational model to investigate how the system responds to changes in a single parameter. To aid this analysis it is convenient to define several metrics which characterise the vascular density profiles. These summary statistics are the maximum amplitude of the vascular density profile (disregarding the limbal vasculature); the location of the vascular front, defined as the location at which the vascular density becomes half-maximal (again disregarding the limbal vasculature); and the area under the vessel density curve, which is representative of the total length of vessels in the cornea (see Figure S2).

Figure S3 summarises the results of our local parameter sensitivity analysis. We vary one

Parameter	Description	Default value and units	Non-dimensional value	Sources
λ_1^f	Maximal rate of FGF-induced dematuration.	0.0187 [h ⁻¹]	0.096	[S9].
χ_f	Chemotactic sensitivity of sprout tips to bFGF.	3.72 [m ² h ⁻¹ M ⁻¹]	0.0191	As in Table S4.
α_0^f	Maximal rate of FGF-induced tip production per unit vessel length.	179 [tips h ⁻¹ per m of vessel]	0.1833	-
D_f	Diffusion constant for bFGF in cornea.	1.92×10^{-7} [m ² h ⁻¹]	0.9853	[S19, S50, S51]
λ_f	Natural decay constant of bFGF.	0.04 [h ⁻¹]	0.205	[S52, S53]
K_{EC}^f	Maximum rate of reduction in molar <i>bFGF</i> concentration per unit EC density due to FGFR binding.	2.16×10^{-17} [moles of bFGF h ⁻¹ (m of vessel) ⁻¹ litre ⁻¹ m ³]	22.168	[S47, S49, S50].
$f_{\frac{1}{2}}^f$	Concentration of bFGF at which occupation of FGFR receptors is half-maximal.	4.22×10^{-11} [M]	0.0422	[S47].
P_f	Permeability of corneal vasculature to bFGF.	1×10^{-4} [m h ⁻¹]	0.513	[S43].
θ_f	Binding constant.	50	50	-
k_p^f	Effective permeability of the cornea-pellet boundary to bFGF.	3.95×10^{-7} [m h ⁻¹]	2.028e-03	-
λ_p^f	Natural decay constant of bFGF in the pellet.	0.04 [h ⁻¹]	0.205	Assume $\lambda_p^f = \lambda_f$.
$[F_T]_{init}$	Initial concentration of bFGF in pellet.	4.92×10^{-5} [M]	4.92×10^4	Hoffmann-La Roche, Penzberg.

Table S5: List of additional parameters required for the simulation of bFGF-induced angiogenesis.

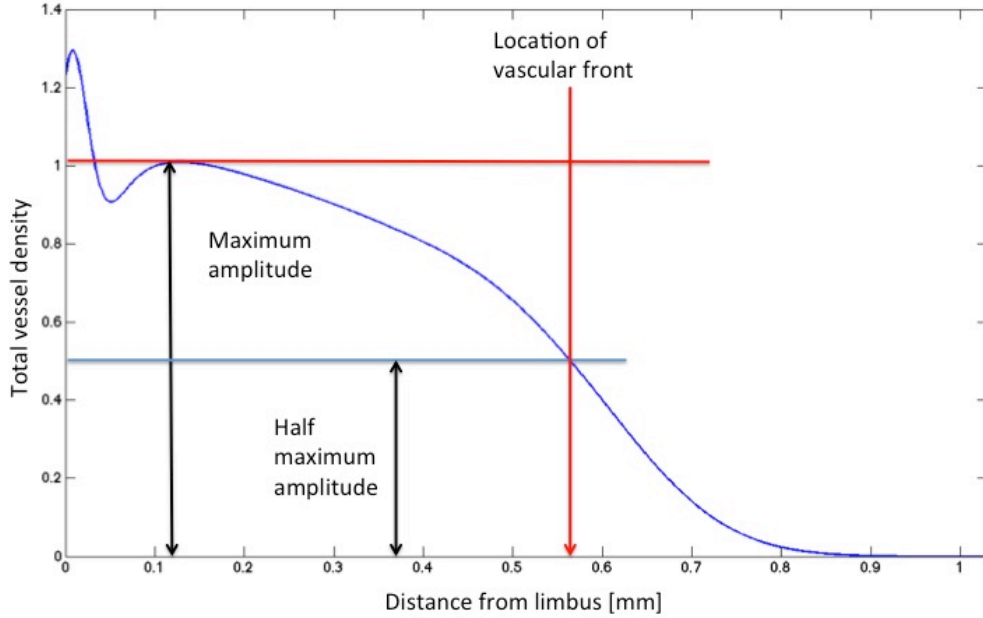


Figure S2: Summary statistics for vascular density profiles. We characterise vessel density profiles using the location of the vascular front, the maximum amplitude of the neovascular wavefront and the area under the vessel density curve.

Parameter	Fold increase in parameter value w.r.t. default values			
	Variant 1	Variant 2	Variant 3	Variant 4 (Default)
λ_1^f	1.84	2.00	1.84	1
α_0^f	4.00	1.19	4.00	1
χ_f	0.88	1.04	0.88	1

Table S6: Parameter modifications for the four variants of our model, (S31)-(S40). For each variant λ_1^f , α_0^f and χ_f are changed w.r.t. their default values (Table S5) to ensure that the simulation results remain faithful to the data arising from experiments in which angiogenesis is induced by bFGF pellets only. All fold changes are correct to 2 d.p.

parameter at a time, keeping all others fixed at their default values. We increase/decrease the value of each parameter by 5%, and simulate the model for each choice of parameter values. We use the simulation results to calculate a central difference approximation to the normalised sensitivities of our chosen summary statistics. For example, we calculate the normalised sensitivity of the area under the vessel density curve, A , to parameter, p as

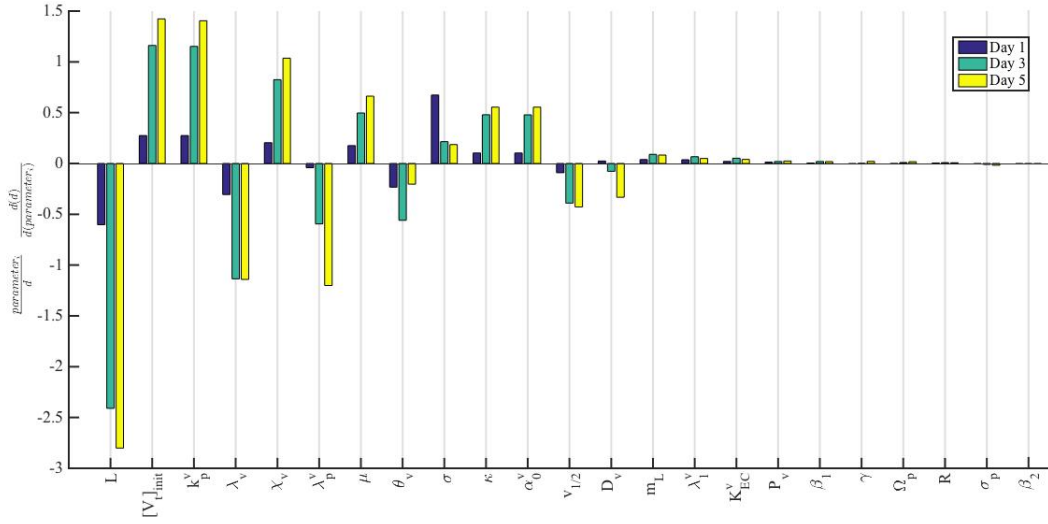
$$\text{normalised sensitivity} = \frac{p_0}{A(p_0)} \left(\frac{\partial A}{\partial p} \right)_{\mathbf{q}_0} \approx \frac{p_0}{A(p_0)} \frac{A(p_0 + \Delta p_0) - A(p_0 - \Delta p_0)}{2\Delta p_0},$$

where the subscript, \mathbf{q}_0 , indicates that the difference is calculated around the point \mathbf{q}_0 in parameter space. We present the normalised sensitivity analysis for the vascular front location (Figure S3a), the maximum amplitude of the vascular wavefront (Figure S3b) and the area under the vessel density curve (Figure S3c) on days 1, 3 and 5 of dimensional simulation time to illustrate how the sensitivity of the system to different parameters changes over time. Such local sensitivity analysis techniques are useful for identifying trends and also for uncovering potential weaknesses in models. That is, the analysis can help convince us that our model is behaving reasonably. For instance, initially increases in D_v lead to increases in tip migration. This is because increasing D_v exposes the limbal vessels to increased levels of VEGF-A₁₆₅ at early times, which promotes increased dematuration and allows for migration towards the pellet at an earlier time than if D_v were less. Meanwhile, at later time-points, model behaviour is dominated by other effects. Namely, on days 3 and 5, increases in D_v increase the maximum amplitude of the vessel density (Figure S3b), and reduce the migration rate of sprout tips (Figure S3a). This behaviour can be explained as follows. Increases in D_v increase VEGF-A₁₆₅ levels across the model domain and decrease its spatial gradient, promoting tip production and reducing the chemotactic stimulus, respectively.

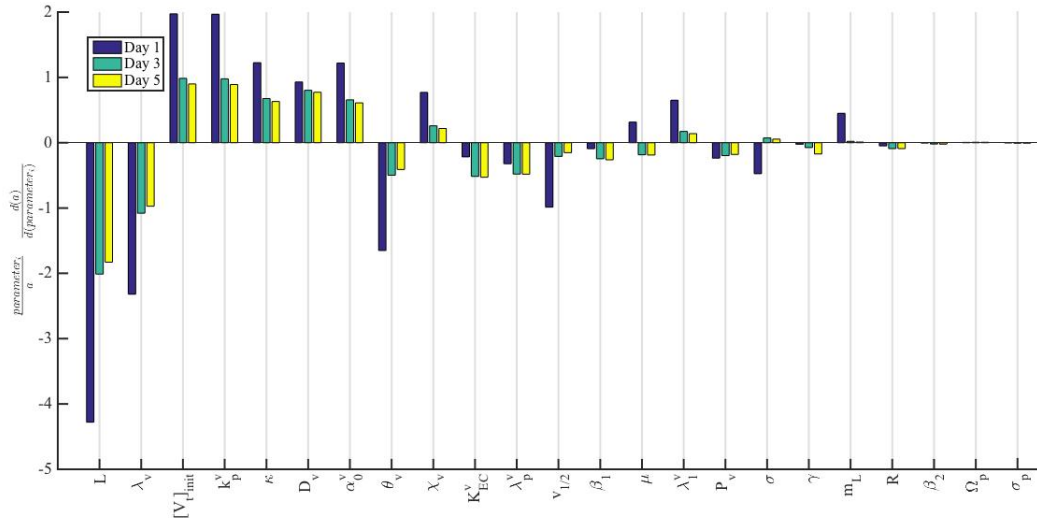
Our sensitivity analysis indicates which parameters may significantly influence the outcomes of our model simulations. Notably, model outputs appear to be most sensitive to changes in parameters affecting VEGF-A₁₆₅ availability (e.g. L , D_v , λ_v , θ_v , k_p^v , λ_p^v and $[V]_t^{init}$) and the response of ECs to VEGF-A₁₆₅ (e.g. χ_v , α_0^v and κ). The model predicts, in particular, that the neoangiogenic response of the limbal vessels is highly sensitive to L , the distance between the pellet and the limbal vessels, with our simulation results being approximately twice as sensitive to variations in L than to any other parameter. This is as discussed in the main manuscript.

6 Numerical convergence

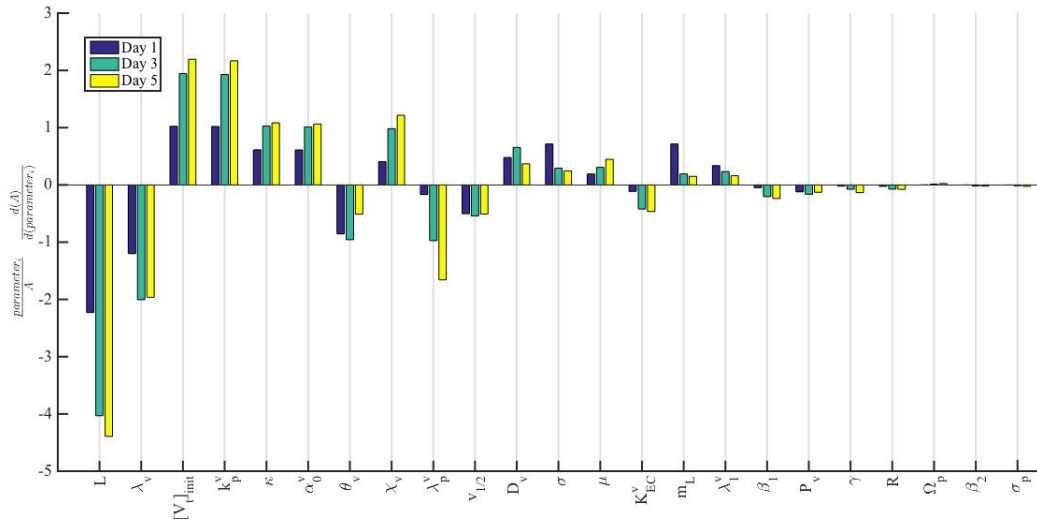
The accuracy of the numerical solutions is sensitive to the resolution of the spatial discretisation. Figure S4 shows how the location of the vascular front changes as the number of spatial nodes is



(a) Normalised sensitivity of the location of the advancing vascular wavefront, d .



(b) Normalised sensitivity of the amplitude of the advancing vascular wavefront, a .



(c) Normalised sensitivity of the area under the vascular density curve, A .

Figure S3: Normalised sensitivity of model output summary statistics in response to local changes in parameter values.

increased when VEGF- A_{165} -induced angiogenesis is simulated using default parameter values. As the resolution of the spatial mesh is increased, sprout tips decrease their rate of migration. The distance that the tips migrate converges to a finite value as the number of nodes is increased. The amplitude of the vascular wavefront also converges to a finite value as the number of nodes is increased. We use a spatial grid with 300 nodes as default for all simulations since this provides a good level of accuracy whilst producing results within reasonable time-scales.

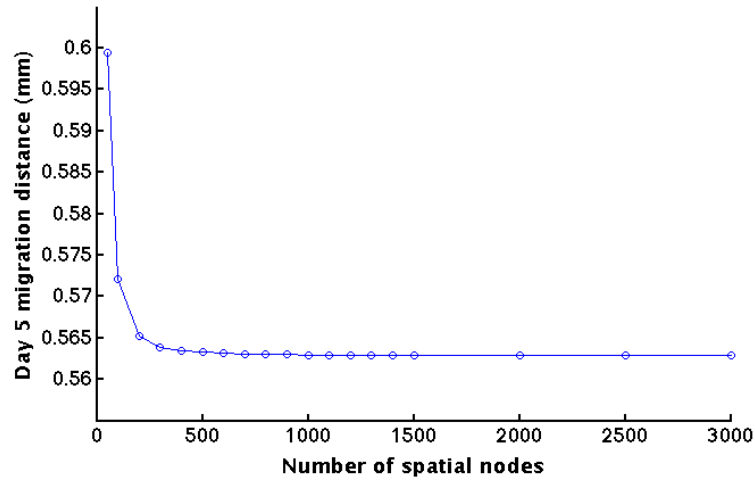


Figure S4: As the number of spatial nodes is increased the rate of migration of sprout tips decreases, converging on a finite value.

References

- [S1] Rogers M.S., Birsner A.E., and D'Amato R.J. 2007. The mouse cornea micropocket angiogenesis assay. *Nat. Protoc.* **2**, 2545–2550. (DOI 10.1038/nprot.2007.368.)
- [S2] Chaudhuri S., Chatterjee S., Katz N., Nelson M., and Goldbaum M. 1989. Detection of blood vessels in retinal images using two-dimensional matched filters. *IEEE T. Med. Imaging* **8**, 263–269. (DOI 10.1109/42.34715.)
- [S3] Al-Rawi M., Qutaishat M., and Arrar M. 2007. An improved matched filter for blood vessel detection of digital retinal images. *Comput Biol. Med.* **37**, 262–267. (DOI 10.1016/j.combiomed.2006.03.003.)
- [S4] Chanwimaluang T. and Fan G. 2003. An efficient blood vessel detection algorithm for retinal images using local entropy thresholding. *Proceedings of the 2003 International Symposium on Circuits and Systems. ISCAS '03*. (DOI 10.1109/ISCAS.2003.1206162.)
- [S5] Zhang E., Schrunder S., and Hoffmann F. 1996. Orthotropic corneal transplantation in the mouse: a new surgical technique with minimal endothelial cell loss. *Graefes Arch. Clin. Exp.* **243** 714–719. (DOI 10.1007/BF00292359.)
- [S6] Song J., Lee Y.G., and Houston J. 2003. Neonatal Corneal Stromal Development in the Normal and Lumican-Deficient Mouse. *Invest. Opth. Vis. Sci.* **44**, 548–557. (DOI 10.1167/iovs.02-0592.)
- [S7] <http://dx.doi.org/10.6084/m9.figshare.1205083>.
- [S8] <http://dx.doi.org/10.6084/m9.figshare.1176779>.
- [S9] Zheng X., Koh G.Y., and Jackson T. 2013. A continuous model of angiogenesis: initiation, extension, and maturation of new blood vessels modulated by vascular endothelial growth factor, angiopoietins, platelet-derived growth factor-B, and pericytes. *Discrete Cont. Dyn-B* **18**, 1109–1154. (DOI 10.3934/dcdsb.2013.18.1109.)
- [S10] Cao R., Bråkenhielm E., Pawliuk R., Wariaro D., Post M.J., Wahlberg E., Leboulch P., and Cao Y. 2003. Angiogenic synergism, vascular stability and improvement of hind-limb ischemia by a combination of PDGF-BB and FGF-2. *Nat. Med.* **9**, 604–613. (DOI 10.1038/nm848.)
- [S11] Hall A. 2006. Review of the Pericyte during Angiogenesis and its Role in Cancer and Diabetic Retinopathy. *Toxicol. Pathol.* **34**, 763–775. (DOI 10.1080/01926230600936290.)
- [S12] Balding D. and McElwain D. 1985. A mathematical model of tumour-induced capillary growth. *J. Theor. Biol.* **114**, 53–73. (DOI 10.1016/S0022-5193(85)80255-1.)
- [S13] Byrne H.M. and Chaplain M.A.J. 1996. Explicit solutions of a simplified model of capillary sprout growth during tumor angiogenesis. *Appl. Math. Lett.* **9**, 69–74. (DOI 10.1016/0893-9659(95)00105-0.)
- [S14] Benjamin L.E., Golijanin D., Itin A., Pode D., and Keshet E. 1999. Selective ablation of immature blood vessels in established human tumors follows vascular endothelial growth factor withdrawal. *J. Clin. Invest.* **103**, 159–166. (DOI 10.1172/JCI5028.)
- [S15] Murakami M. and Sakurai T. 2012. Role of fibroblast growth factor signaling in vascular formation and maintenance: orchestrating signaling networks as an integrated system. *Wiley Interdisciplinary Reviews: Systems Biology And Medicine* **4**, 615–629. (DOI 10.1002/wsbm.1190.)

- [S16] Murakami M., Nguyen L.T., Hatanaka K., Schachterle W., Chen P.Y., Zhuang Z.W., Black B.L., and Simons M. 2011. FGF-dependent regulation of VEGF receptor 2 expression in mice. *J. Clin. Invest.* **121**, 2668–2678. (DOI 10.1172/JCI44762DS1.)
- [S17] Seghezzi G., Patel S., Ren C.J., Gualandris A., Pintucci G., Robbins E.S., Shapiro R.L., Galloway A.C., Rifkin D.B., and Mignatti P. 1998. Fibroblast growth factor-2 (FGF-2) induces vascular endothelial growth factor (VEGF) expression in the endothelial cells of forming capillaries: an autocrine mechanism contributing to angiogenesis. *J. Cell Biol.* **141**, 1659–1673. (DOI 10.1083/jcb.141.7.1659.)
- [S18] Pepper M.S. and Mandriota S.J. 1998. Regulation of vascular endothelial growth factor receptor-2 (Flk-1) expression in vascular endothelial cells. *Exp. Cell Res.* **241**, 414–425. (DOI 10.1006/excr.1998.4072.)
- [S19] Tong S. and Yuan F. 2008. Dose response of angiogenesis to basic fibroblast growth factor in rat corneal pocket assay: II. Numerical simulations. *Microvas. Res.* **75**, 16–24. (DOI 10.1016/j.mvr.2007.09.005.)
- [S20] Akeson A., Herman A., Wiginton D., and Greenberg J. 2010. Endothelial cell activation in a VEGF-A gradient: relevance to cell fate decisions. *Microvas. Res.* **80**, 65–74. (DOI 10.1016/j.mvr.2010.02.001.)
- [S21] Wang D., Lehman R.E., Donner D.B., Matli M.R., Warren R.S., and Welton M.L. 2002. Expression and endocytosis of VEGF and its receptors in human colonic vascular endothelial cells. *Am. J. Physiol-Gastr. L.* **282**, G1088–G1096. (DOI 10.1152/ajpgi.00250.2001.)
- [S22] Augustin H.G., Young Koh G., Thurston G., and Alitalo K. 2009. Control of vascular morphogenesis and homeostasis through the angiopoietin–Tie system. *Nat. Rev. Mol. Cell Bio.* **10**, 165–177. (DOI 10.1038/nrm2639.)
- [S23] Gevertz J.L. and Torquato S. 2006. Modelling the effects of vasculature evolution on early brain tumour growth. *J. Theor. Biol.* **243**, 517–531. (DOI 10.1016/j.jtbi.2006.07.002.)
- [S24] Plank M.J., Sleeman B.D., and Jones P.F. 2004. A mathematical model of tumour angiogenesis, regulated by vascular endothelial growth factor and the angiopoietins. *J. Theor. Biol.* **229**, 435–454. (DOI 10.1016/j.jtbi.2004.04.012.)
- [S25] Sherratt J.A. and Murray J.D. 1990. Models of epidermal wound healing. *P Roy. Soc. Lond. B Bio.* **241**, 29–36. (DOI 10.1098/rspb.1990.0061.)
- [S26] Stokes C.L., Lauffenburger D.A., and Williams S.K. 1991. Migration of individual microvessel endothelial cells: stochastic model and parameter measurement. *J. Cell Sci.* **99**, 419–430.
- [S27] Kouvroukoglou S., Dee K.C., Bizios R., McIntire L.V., and Zygorakis K. 2000. Endothelial cell migration on surfaces modified with immobilized adhesive peptides. *Biomaterials* **21**, 1725–1733. (DOI 10.1016/S0142-9612(99)00205-7.)
- [S28] Friedl P. and Gilmour D. 2009. Collective cell migration in morphogenesis, regeneration and cancer. *Nat. Rev. Mol. Cell Biol.* **10**, 445–57. (DOI 10.1038/nrm2720.)
- [S29] Addison-Smith, B. 2010. Mathematical Modelling of Tumour-Induced Angiogenesis. PhD thesis. QUT.
- [S30] Owen M.R., Stamper I.J., Muthana M., Richardson G.W., Dobson J., Lewis C.E., and Byrne H.M. 2011. Mathematical modelling predicts synergistic antitumor effects of combining a macrophage based, hypoxia-targeted gene therapy with chemotherapy. *Cancer Res.* **71**, 2826–2837. (DOI 10.1158/0008-5472.CAN-10-2834.)
- [S31] Stokes C.L., Rupnick M.A., Williams S.K., and Lauffenburger D.A.. 1990. Chemotaxis of human microvessel endothelial cells in response to acidic fibroblast growth factor. *Lab. Invest.* **63**, 657–68.

- [S32] Muthukkaruppan V.R., Kubai L., and Auerbach R. 1982. Tumor-induced neovascularization in the mouse eye. *J Natl. Cancer I.* **69**, 699–708. (DOI 10.1093/jnci/69.3.699.)
- [S33] Folkman J. and Klagsbrun M. 1975. Tumor angiogenesis: effect on tumor growth and immunity. *Fundamental Aspects of Neoplasia*. Springer, Berlin, Heidelberg, 401–412.
- [S34] Bentley K., Mariggi G., Gerhardt H., and Bates P.A. 2009. Tipping the Balance: Robustness of Tip Cell Selection, Migration and Fusion in Angiogenesis. *PLoS Comp. Biol.* **5**, e1000549. (DOI 10.1371/journal.pcbi.1000549.t004.)
- [S35] Tong S. and Yuan F. 2008. Dose response of angiogenesis to basic fibroblast growth factor in rat corneal pocket assay: I. Experimental characterizations. *Microvas. Res.* **75**, 10–15. (DOI 10.1016/j.mvr.2007.06.002.)
- [S36] Sholley M.M., Ferguson G.P., Siebel H.R., Montour J.L., and Wilson J.D. 1984. Mechanisms of neovascularization. Vascular sprouting can occur without proliferation of endothelial cells. *Lab. Invest.* **51**, 624–634.
- [S37] Chen R.R., Silva E.A., Yuen W.W., and Mooney D.J. 2006. Spatio-temporal VEGF and PDGF Delivery Patterns Blood Vessel Formation and Maturation. *Pharm. Res.* **24**, 258–264. (DOI 10.1007/s11095-006-9173-4.)
- [S38] MacGabhann F. 2005. Differential binding of VEGF isoforms to VEGF receptor 2 in the presence of neuropilin-1: a computational model. *Am. J. Physiol-Heart C.* **288**, H2851–H2860. (DOI 10.1152/ajp-heart.01218.2004.)
- [S39] Ambrosi D., Bussolino F., and Preziosi L. 2005. A Review of Vasculogenesis Models. *J. Theor. Med.* **6**, 1–19. (DOI 10.1080/1027366042000327098.)
- [S40] Serini G., Ambrosi D., Giraudo E., Gamba A., Preziosi L., and Bussolino F. 2003. Modelling the early stages of vascular network assembly. *The EMBO Journal* **22**, 1771–1779. (DOI 10.1093/emboj/cdg176.)
- [S41] MacGabhann F. and Popel A.S. 2003. Model of competitive binding of vascular endothelial growth factor and placental growth factor to VEGF receptors on endothelial cells. *Am. J. Physiol-Heart C.* **286**, 153H–164. (DOI 10.1152/ajpheart.00254.2003.)
- [S42] Bikfalvi A., Sauzeau C., Moukadiri H., Maclouf J., Busso N., Bryckaert M., Plouet J., and Tobelem G. 1991. Interaction of vasculotropin/vascular endothelial cell growth factor with human umbilical vein endothelial cells: binding, internalization, degradation, and biological effects. *J. Cell. Physiol.* **149**, 50–59. (DOI 10.1002/jcp.1041490108.)
- [S43] Fu B.M. and Shen S. 2003. Structural mechanisms of acute VEGF effect on microvessel permeability. *Am. J. Physiol-Heart C.* **284**, H2124–H2135. (DOI 10.1152/ajpheart.00894.2002.)
- [S44] Stefanini M.O., Wu F.T., Mac Gabhann F., and Popel A.S. 2008. A compartment model of VEGF distribution in blood, healthy and diseased tissues. *BMC Syst. Biol.* **2**, 77. (DOI 10.1186/1752-0509-2-77.)
- [S45] Tsai P.S., Kaufhold J.P., Blinder P., Friedman B., Drew P.J., Karten H.J., Lyden P.D., and Kleinfeld D. 2009. Correlations of neuronal and microvascular densities in murine cortex revealed by direct counting and colocalization of nuclei and vessels. *J. Neurosci.* **29**, 14553–14570. (DOI 10.1523/JNEUROSCI.3287-09.2009.)
- [S46] Peebo B.B., Fagerholm P., Traneus-Rockert C., and Lagali N. 2011. Time-lapse in vivo imaging of corneal angiogenesis: the role of inflammatory cells in capillary sprouting. *Invest. Ophthalm. Vis. Sci.* **52**, 3060–3068. (DOI 10.1167/iovs.10-6101.)

- [S47] Bikfalvi A., Dupuy E., Inyang A.L., Fayein N., Leseche G., Courtois Y., and Tobelem G. 1989. Binding, internalization, and degradation of basic fibroblast growth factor in human microvascular endothelial cells. *Exp. Cell Res.* **181**, 75–84. (DOI 10.1016/0014-4827(89)90183-3.)
- [S48] Moscatelli D. 1988. Metabolism of receptor-bound and matrix-bound basic fibroblast growth factor by bovine capillary endothelial cells. *J. Cell Biol.* **107**, 753–759. (DOI 10.1083/jcb.107.2.753.)
- [S49] Fannon M., Forsten-Williams K., Dowd C.J., Freedman D.A., Folkman J., and Nugent M.A. 2003. Binding inhibition of angiogenic factors by heparan sulfate proteoglycans in aqueous humor: potential mechanism for maintenance of an avascular environment. *The FACEB Journal* **17**, 902–904. (DOI 10.1096/fj.02-0935fje.)
- [S50] Filion R.J. and Popel A.S. 2004. A reaction-diffusion model of basic fibroblast growth factor interactions with cell surface receptors. *Ann. Biomed. Eng.* **32**, 645–663. (DOI 10.1023/B:ABME.0000030231.88326.78.)
- [S51] Boyer P.M. and Hsu J.T. 1992. Experimental studies of restricted protein diffusion in an agarose matrix. *AIChE J.* **38**, 259–272.
- [S52] Westall F.C., Rubin R., and Gospodarowicz D. 1983. Brain-derived fibroblast growth factor: a study of its inactivation. *Life Sci.* **33**, 2425–2429. (DOI 10.1016/0024-3205(83)90636-7.)
- [S53] Sperinde G.V. and Nugent M.A. 1998. Heparan sulfate proteoglycans control intracellular processing of bFGF in vascular smooth muscle cells. *Biochemistry* **37**, 13153–13164. (DOI 10.1021/bi980600z.)
- [S54] Dowd C.J., Cooney C.L., and Nugent M.A. 1999. Heparan sulfate mediates bFGF transport through basement membrane by diffusion with rapid reversible binding. *J. Biol. Chem* **274**, 5236–5244. (DOI 10.1074/jbc.274.8.5236.)
- [S55] Shampine L.F. and Reichelt M.W. 1997. The MATLAB ODE suite. *SIAM J. Sci. Comput.* **18**, 1–22. (DOI 10.1137/S1064827594276424.)